THESIS FOR THE DEGREE OF DOCTOR OF PHILOSOPHY

Development of syntheses for nanostructured titania and silica

Gunnar Símonarson

Department of Chemistry and Chemical Engineering
CHALMERS UNIVERSITY OF TECHNOLOGY
Gothenburg, Sweden 2019

Development of syntheses for nanostructured titania and silica

Gunnar Símonarson
ISBN 978-91-7905-159-4

Doktorsavhandlingar vid Chalmers Tekniska Högskola
Ny serie nr. 4626
ISSN 0346-718X

Department of Chemistry and Chemical Engineering
Chalmers University of Technology
SE-412 96 Gothenburg
Sweden
Telephone +46 (0)31-772 1000

Cover:
The background shows a TEM image of mesoporous titania. The crystal structure of titania anatase polymorph (reproduced from reference 22) is shown in front.

Printed at Chalmers Reproservice
Gothenburg, Sweden 2019

Development of syntheses for nanostructured titania and silica

Gunnar Símonarson

Department of Chemistry and Chemical Engineering
Chalmers University of Technology

ABSTRACT

Nanostructured TiO_2 is of great interest for a variety of energy and environmental applications, including conversion of solar energy, for energy storage systems and removal of organic pollutants in water and air. Titania is composed of earth abundant elements, it is environmentally friendly and chemically stable which makes it an attractive material to utilize. For many of the applications of titania, high surface area is beneficial, and it can be achieved by designing materials with structural features in the nanometer range, e.g. particles of a few nanometer in diameter and mesoporous materials with pore diameters in the range of 2-50 nm. In addition, the degree of crystallinity and the polymorph type have large effects on the physicochemical properties of the material.

In this work, syntheses of titania nanoparticles and mesoporous titania and silica films were developed and the effect of varying relevant synthesis parameters on the structure on the atomic and nanometer scale was investigated. A low-temperature spray deposition method was developed to prepare ordered mesostructured titania and silica films via evaporation induced self-assembly (EISA) process, using a non-ionic block copolymer as a structure directing agent. The spray deposition method can be scaled up, the film thickness is tunable, surfaces of various shapes can be coated and heat sensitive substrates can be used. For the preparation of the mesoporous titania films, the polymer template was removed with UV radiation and the synthesis is carried out completely at temperatures below 50 °C. The effect of synthesis parameters, such as film thickness, synthesis time and aging time at high relative humidity on the structure at the atomic and nanometer scale were studied. Moreover, the prepared mesoporous titania was examined as an anode material in lithium ion batteries and the lithiation was studied in detail with electrochemical methods and structural characterization methods.

In addition, titania nanoparticles were synthesized under acidic conditions at low temperature and the polymorph selectivity studied. Unexpectedly, selectivity towards rutile was observed with short synthesis time and related to high concentration of the titania precursor, whereas the selectivity towards brookite and anatase was related to lower concentrations of the precursor.

Key words: *Titanium dioxide, mesoporous titania, mesoporous silica, nanoparticles, spray deposition, lithium intercalation, X-ray characterization.*

LIST OF PUBLICATIONS

This thesis is based on the work described in the following papers.

1. Evolution of the polymorph selectivity of titania formation under acidic and low-temperature conditions
   Gunnar Símonarson, Sanna Sommer, Antiope Lotsari, Björn Elgh and Anders E.C. Palmqvist
   ACS Omega 2019, 4, 5750-5757.

2. Low-temperature spray deposition synthesis of locally ordered mesoporous polycrystalline titania films
   Gunnar Símonarson, Antiope Lotsari and Anders E.C. Palmqvist
   Under review in Microporous and Mesoporous Materials

3. Electrochemical and structural characterization of lithiation in spray deposited ordered mesoporous titania as anode for Li ion batteries
   Gunnar Símonarson, Giulio Calcagno, Antiope Lotsari and Anders. E.C. Palmqvist
   Manuscript submitted to Journal of Materials Chemistry A

4. Preparation of ordered mesoporous silica films by low-temperature spray deposition
   Gunnar Símonarson, Antiope Lotsari and Anders E.C. Palmqvist
   Manuscript

CONTRIBUTION REPORT

1. Responsible for material synthesis. Partly responsible for XRD and TEM measurements and data analysis. Responsible for writing the manuscript.

2. Responsible for all experimental work, SAXS measurements and data analysis. Partly responsible for TEM measurements. Responsible for writing the manuscript.

3. Responsible for XAS measurement and jointly responsible for all electrochemical measurements, TEM measurements and data analysis. Responsible for writing the manuscript.

4. Responsible for all experimental work, SAXS measurements and data analysis. Partly responsible for TEM measurements. Responsible for writing the manuscript.

TABLE OF CONTENTS

"I leave Sisyphus at the foot of the mountain. One always finds one's burden again. But Sisyphus teaches the higher fidelity that negates the gods and raises rocks. He too concludes that all is well. This universe henceforth without a master seems to him neither sterile nor futile. Each atom of that stone, each mineral flake of that night-filled mountain, in itself, forms a world. The struggle itself toward the heights is enough to fill a man's heart. One must imagine Sisyphus happy."

Albert Camus, The myth of Sisyphus

1. INTRODUCTION

With growth in the human population and increased standard of living for the general public, mankind has an ever increasing demand for energy. Today more than 80% of the world energy production comes from fossil fuels, such as coal, oil and natural gas, and only about 2% comes from solar, wind, hydropower or other renewable energy sources.[1] It is well known that fossil fuels are a limited source and, in addition, fossil fuel combustion, along with other industrial processes, have led to increasing atmospheric concentration of carbon dioxide which is considered to be the primary human contributor to global warming.[2] Thus, there is a great interest in developing new methods and materials that can help facilitating the vital transition for our society from being dependent on fossil fuels to be able to rely on renewable energy sources.

For this transition to be realized there is a need to better harness intermittent renewable energy sources, such as solar and wind energy, and to develop reliable energy storage systems to deliver the energy efficiently when it is needed. Enormous efforts have been made to develop solutions that increase the efficiency and dependability of renewable energy sources. This includes, but is not limited to, solar cells that convert solar energy to electricity[3–5], fuel cells converting chemical energy to electrical energy[6] and batteries storing and converting chemical energy to electrical energy[7]. To further increase the viability of these solutions in terms of efficiency, stability, price and availability, there is a need to develop energy materials made from non-toxic earth abundant materials.

Titanium dioxide, or titania, consists of two earth abundant elements, titanium is the 9th most abundant element in earth's crust and oxygen is the most abundant element. Titanium is mostly found as oxide minerals, the most common ones being ilmenite ($FeTiO_3$) and rutile (TiO_2).[8] In addition to its high abundance, titania is chemically stable, environmentally friendly and non-toxic, which makes it an attractive material to utilize. In 1972, Fujishima and Honda reported

the photoelectrolysis of water on a titanium dioxide electrode that sparked a huge interest in the material.[9] Ever since then, intensive research on titania has resulted in the application of the material in promising energy solutions, such as in devices that convert solar energy to electrical energy[10] and in lithium ion batteries[11], and for environmental applications such as photocatalytic removal of organic pollutants in water and air[12]. These applications take advantage of the unique properties of pure titanium dioxide or in combination with other materials.

Nanostructured titanium dioxide is of special interest due to its exceptional performance in these applications, by offering high surface area which is a considerable advantage.[13] In addition, there are several other important structural properties that affect the material performance, including the degree of crystallinity, the polymorph type and particle size. The titania nanostructures studied in this thesis are titania nanoparticles and mesoporous titania materials.

To prepare mesoporous titania materials with high surface areas, amphiphilic molecules are typically used to give structure to the material in a bottom-up approach.[14] The approach of exploiting the self-assembly of amphiphilic molecules for synthesis of nanostructured materials has, due to the diversity of the amphiphilic molecules and their tunable structure, yielded various sizes and structures of materials of different elemental compositions. Making ordered mesoporous titania materials from the amphiphilic molecules is a multi-step process. The structure is typically achieved with mixing and sometimes with solvent evaporation at low temperatures. Subsequently, in a second step, the structure directing amphiphilic molecule is removed, commonly with a high temperature treatment. During the high temperature treatment, the crystallinity of the material is increased, which is beneficial for certain applications, but a common side effect is that the ordered mesostructure is lost at the temperatures needed to remove the template. Since the ordered mesostructure is beneficial for the material performance there is a large interest in developing low temperature preparation methods for crystalline mesoporous titania.[15,16]

Titania crystallizes mainly in three different atomic arrangements, rutile, brookite and anatase. Anatase and rutile have been thoroughly studied and anatase is generally assumed to be the more photocatalytically active phase while rutile is the thermodynamically stable phase in bulk. Brookite has been less studied, due to general difficulties in preparation, but it is a promising candidate for photocatalytic and battery applications.[17]

In parallel, mesostructured silica materials have received continuous attention since the first reported syntheses in the early 1990's.[18,19] The main reason for this interest from researchers in academia and in industry are the wide range of applications of the material. Mesoporous silica has many of the same characteristics as mesoporous titania, such as high surface area, tunable pore size and ordered pore structure. Ordered mesoporous silica can be prepared as powder in bulk or as mesoporous films which are typically prepared by dip-coating or spin-coating via evaporation induced self-assembly (EISA).

The objective of this work was to contribute to the understanding of low-temperature synthesis of titania nanoparticles and mesoporous titania and silica films and shed light on how synthesis conditions affect the structure of the material on the atomic and nanoscale. In particular, low temperature acidic solution syntheses were studied, where the effects of synthesis time and titania precursor concentration on the polymorph selectivity were investigated. In addition, a low-temperature spray deposition method to prepare ordered mesoporous titania and silica films was developed and the effects of synthesis parameters, such as film thickness, synthesis time and aging time at high relative humidity, on the structure on the atomic and nanometer scale were studied. Moreover, mesoporous titania was evaluated as an anode material for lithium ion batteries and the lithium intercalation and deintercalation processes were examined with electrochemical methods and structural characterization methods.

2. CHEMISTRY OF TITANIA

Titanium dioxide, or titania, is a wide band gap semi-conductor composed of two earth abundant elements, titanium and oxygen. The world's annual production capacity of titania is estimated to be over 7 million tons in 2016 and more than 90% of the titania global production is used as pigment in paint, plastics and paper.[20] The remaining amount is used for catalysis, ceramics and textiles to name a few. Titania scatters light very well over the whole visible range, which gives the material its white color and its high refractive index makes it a good pigment. Titania has been studied and applied in various energy and environmental applications, including solar cells and water and air purification systems. A great advantage of titania is that it is environmentally friendly, photostable, it is not toxic and it is composed of earth abundant elements which makes it attractive to work with. However, the main drawback of the material for photocatalytic applications is that UV light is needed to drive the photocatalytic reactions, but only 5% of the solar energy that reaches the surface of the earth is in the form of UV radiation.[21]

2.1 CRYSTAL STRUCTURES

Titanium dioxide occurs naturally mainly in three different polymorphs, rutile, brookite and anatase shown in Figure 1.

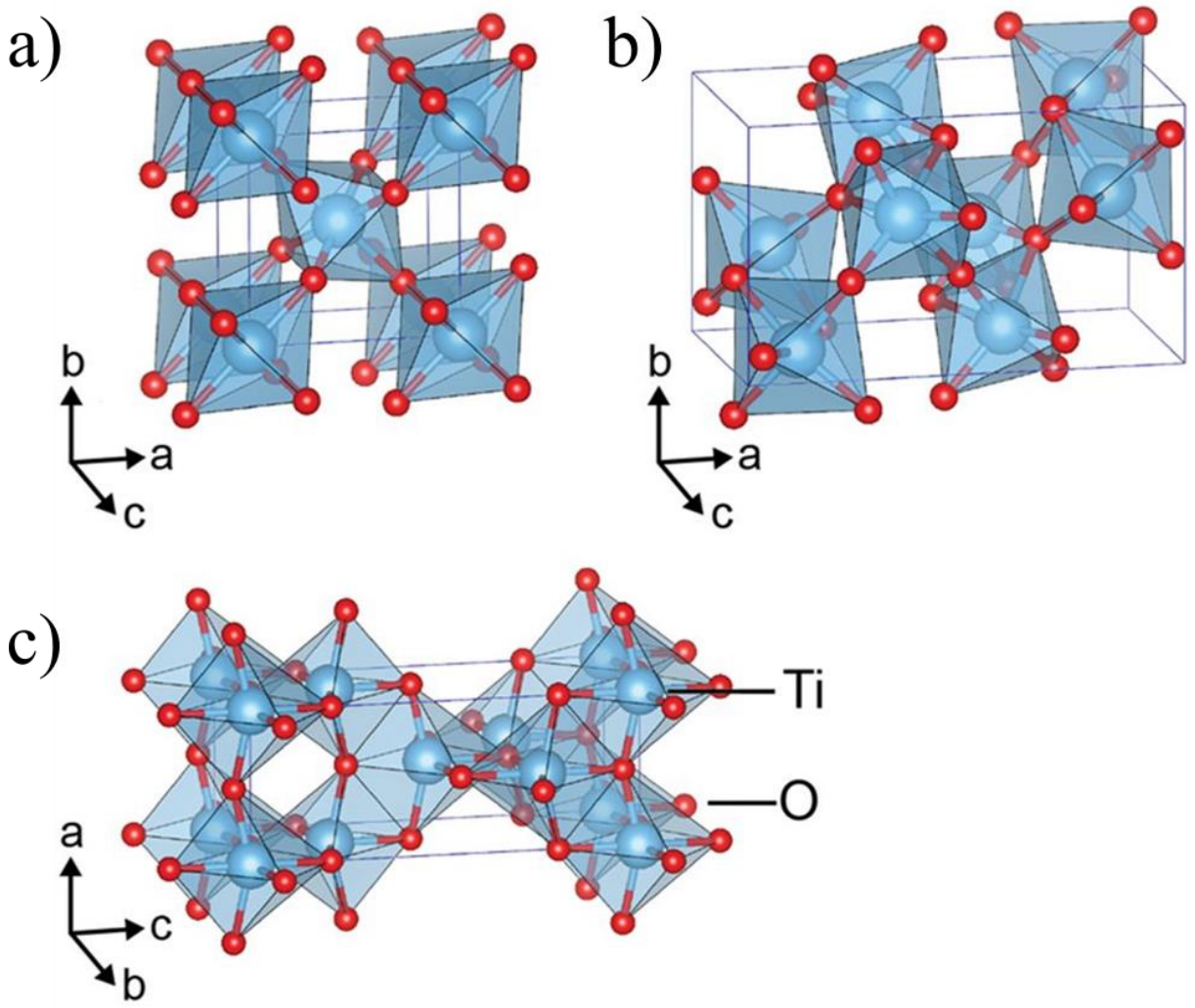

Figure 1. The three main polymorphs of titania, rutile (a), brookite (b) and anatase (c). Reproduced from reference [22].

Rutile has a tetragonal unit cell, space group $P4_2/mnm$, where each titanium atom is coordinated with six oxygen atoms and each oxygen atom is coordinated with 3 titanium atoms. It can be described as a distorted TiO_6 octahedra where each octahedra shares two equatorial edges. The unit cell is composed of titanium atoms on the corners and one in the center, two oxygen atoms in plane with the centered titanium atom, two oxygen atoms in opposite quadrants of the top face and two oxygen atoms directly below in the bottom face. Rutile is the most compact of the three naturally occurring crystalline phases and has a band gap of 3.0 eV.[23]

Anatase also has a tetragonal unit cell, space group $I4_1/amd$, and each titanium atom is coordinated with six oxygen atoms and each oxygen atom is coordinated with 3 titanium atoms and just as the rutile structure it can be described as a distorted TiO_6 octahedra but which shares four edges. Anatase has a more open structure than rutile and has a band gap of 3.2 eV.[24]

Brookite has a unit cell which is orthorhombic, space group Pbca, and like the other polymorphs, the structure is described as a distorted octahedra, with 6 oxygen atoms surrounding a titanium atom. It has been less studied than the other two naturally occurring polymorphs, mainly due to challenges in synthesizing it. Reports on the bandgap of brookite vary, but it is generally assumed to be between the values of rutile and anatase.[25,26]

Controlling the crystallinity and the polymorph distribution is of high importance for application-targeted material design. In terms of photocatalytic activity, it is generally accepted that anatase is more active than rutile[27], but a combination of these two phases has been shown to be more active than pristine samples of either polymorph[28,29]. A suggested explanation for this lies in the band alignment of the two polymorphs. The conduction band of rutile lies above the conduction band of anatase, and from computational and experimental evidence it has been proposed that photo-excited electrons in the conduction band of the rutile polymorph can spill over to the lower energy conduction band of the anatase polymorph aiding the separation of the electrons and holes, and improving the photocatalytic activity of the material.[30,31] The photocatalytic activity of brookite phase has been less studied than that of rutile and anatase, and it is disputed how it compares to the two polymorphs. Some studies suggest that the activity is lower than anatase, and other suggest that it is similar[32,33] or higher[34,35]. Therefore, it is of high importance to control the phase composition of titania materials and understand how the synthesis parameters influence the crystal phase selectivity.

Some other titania polymorphs have been reported, including TiO_2-B phase which has a more open structure than both the anatase and the rutile polymorphs. It has been shown to be naturally occurring in small quantities along with the anatase phase.[36] The phase was first synthesized by Marchand et al. in 1980 in a high temperature solid state reaction, but later it has also been prepared from hydrothermal treatment of anatase TiO_2 under highly basic conditions.[37,38] The B phase has not been identified in any of the synthesis studied during the work with this thesis.

2.1.1 THERMODYNAMIC STABILITY

In bulk titania, rutile is the thermodynamically stable polymorph but both anatase and brookite are kinetically stable at room temperature.[39] The anatase and brookite polymorphs are converted to rutile at high temperatures, the considered transformation temperature in bulk materials is around 600 °C in air.[40,41] The transformation temperature of nanostructured materials has been reported to be somewhat lower. Additionally, it has been suggested that the relative thermodynamic stability of the polymorphs is size-dependent for crystallites when the size is of a few tenths of nanometers. Banfield et al. suggested that anatase is the most stable

polymorph for crystallites below 11 nm, and brookite is the most stable polymorph between 11 and 35 nm. This is due to rutile having a larger surface free energy than the other two phases which naturally becomes more important at small crystallite sizes, where the ratio of atoms on the surface versus in the bulk is large.[39,41]

2.2 HYDROLYSIS AND CONDENSATION REACTIONS

Syntheses of nanostructured TiO_2 are usually achieved using either inorganic precursors, such as $TiCl_4$, or organic titanium alkoxide precursors. Both types of precursors are easily hydrolyzed in water, and the hydrolyzed species condensate to TiO_2. The type of TiO_2 formed (amorphous or different polymorph phases) is affected by thermodynamics as well as relative kinetics of available condensation pathways, which in turn are influenced by the type of hydrolyzed species that form in the solution and the conditions employed. Several factors, such as pH, temperature, the type of precursor and the precursor concentration impact the distribution of hydrolyzed species and the relative kinetics of condensation.[42]

Upon adding the titania precursor species to water it is hydrolyzed, the hydrolysis occurs easily so care should be taken to avoid moisture entering the chemical bottles when they are stored. The nucleophilic water molecules are attracted to the electrophilic titanium atom. When titanium alkoxide precursors are hydrolyzed, a nucleophilic substitution occurs including a proton transfer from the attacking water molecule to the alkoxy group, and a removal of the protonated group. This hydrolysis is catalyzed under acidic conditions, where the alkoxy group can be protonated by the free protons in the medium:

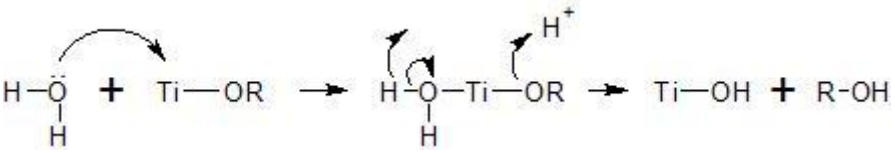

(1)

When the precursor is hydrolyzed, different ligands will be present, mainly depending on the acidity of the solution. The equilibrium between the ligands is given with:

$$[Ti(OH_2)] \rightleftharpoons [Ti - OH] + H^+ \rightleftharpoons [Ti = O] + 2H^+ \quad (2)$$

Under acidic conditions the equilibrium lies to the left in the reaction scheme presented above, favoring the OH_2 ligand, also known as the aquo group. Under intermediate conditions the

equilibrium lies closer to the middle and the hydroxo groups, OH, become more apparent. In alkaline conditions, the oxo ligands, =O, will be more dominant.[42] Condensation of the precursor may occur by three different competitive pathways: alcoxolation, oxolation and olation. Alcoxolation occurs when a Ti-OH attacks a titanium alkoxide species, resulting in the formation of a Ti-O-Ti bridge and elimination of the alcohol. The mechanism is similar to the hydrolysis reaction shown in equation (1), but where a titanium atom replaces one of the protons in the nucleophile.[43]

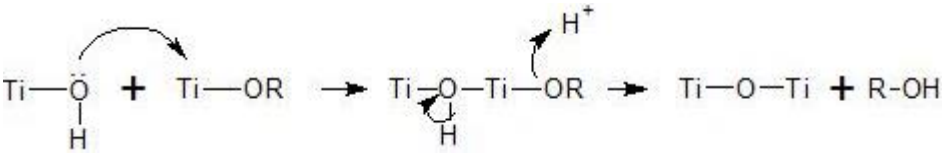

(3)

Oxolation occurs by a similar mechanism as alcoxolation, but where the leaving group is water.

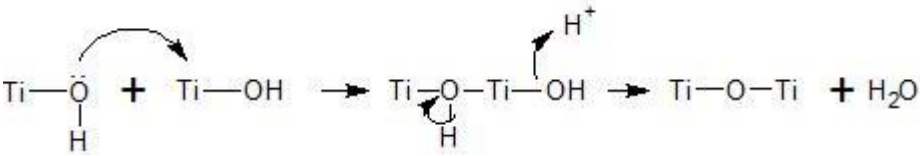

(4)

Olation occurs when a hydroxy bridge is formed between two metal centers. In a fully hydrolyzed and fully coordinated titanium complex, olation proceeds via substitution mechanism where a hydroxy group is the nucleophile and a water molecule is the leaving group. The reaction mechanism for olation is commonly given as:

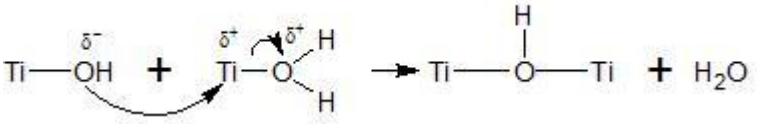

(5)

However, to achieve full condensation to TiO_2 the proton on the hydroxyl bridge must be released and the full condensation becomes:

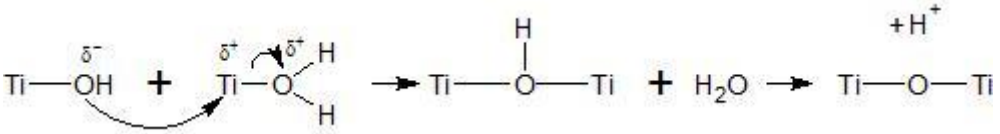

(6)

In solutions with high water to titania precursor ratio, the alkoxide precursor may be fully hydrolyzed, and at low pH environment, where a high concentration of aquo groups will be present, olation is presumably the dominating condensation pathway.[42,43] In this case, protons will be released as the condensation reaction proceeds. The protons released will then lower the pH in the solution as well as push the equilibrium in equation (2) further to the left, favoring the aquo ligands. This was indeed observed with pH measurements shown in **Paper 1**. Furthermore, in a more acidic environment, where the concentration of aquo groups is higher, the condensation rate will decrease due to lack of nucleophilic hydroxo groups contributing to a lower rate of titania particle formation.

The structure of the synthesized titania product depends on the relative rates of the four reactions: hydrolysis, oxolation, alcoxolation and olation. Acidity influences the reactions and in turn, affects the structure of the titania. Under acidic conditions, access to protons makes the alkoxide a better leaving group which increases the hydrolysis rate. High water to titanium precursor ratio results in complete hydrolysis of the titanium alkoxide, and the same hydrolyzed species can be formed with inorganic and organic alkoxide precursors. Other parameters such as the type of alkoxy group, the hydrolysis ratio ($h=n_{H_2O}/n_{alkoxide}$) and the concentration of the precursor affect the relative rates of the reactions.[42] Additionally, under acidic conditions the more dominating presence of the aquo group will decrease the rate of the condensation reactions. The subsequent oligomerization and nucleation of the titania particles are discussed in the following section.

In **Paper 1**, we report a synthesis procedure, carried out at low temperature and at low pH, which results nanoparticles formation with selectivity towards the rutile polymorph at high precursor concentration, but towards brookite at low precursor concentration.[44] Synthesis of phase pure brookite remains a challenge as the mechanistic understanding of the synthesis is not well established and in comparison to anatase and rutile, the brookite polymorph rarely forms phase pure. However, it has been reported that the presence of sodium ions is necessary for brookite formation [45], and the selective crystallization of titania has been previously related to a balance between pH, titania precursor concentration and Cl^- ion concentration.[46]

2.3 NUCLEATION

In addition to the hydrolysis and condensation of the monomeric titania species, the nucleation and polymerization is important. Titanium clusters form during the nucleation stage and serve as building blocks in the formation of titania particles. The type of titanium clusters formed

influences the properties of the final product, the titania particles, and identification of these clusters during the nucleation process is therefore of interest. The polycondensation mechanisms have been thoroughly studied for silicon alkoxides, but much less for transition metal oxides. The studies that exist have shown that the nature of the titanium clusters formed is influenced by the type of alkoxy groups, pH and hydrolysis ratio (h).[47] In these studies it was reported that for pH=2.7, the building blocks prepared with titanium ethoxide contain 6-7 titanium atoms, compared to the 10-12 titanium atoms containing building blocks observed when prepared from titanium iso-propoxide or titanium butoxide.[47] When studied in the pH range from 3-10 the mass spectra remained very similar, with some variations in the intensity distribution. At low pH, protonation of the hydroxyl groups retards the polycondensation reactions by hindering nucleophilic attack on Ti, and also hinders aggregation due to repulsion forces between the building blocks.[48] In these studies, the reaction solution had to be diluted before introducing it to the mass spectrometer to avoid clogging of the capillary. After the dilution the concentration of soluble titania precursor in the solution that was introduced to the mass spectrometer was very low (<1.5 mM). Much remains unclear on the nucleation and growth of titania structures, partly due to challenges in finding appropriate methods to study the process in-situ.

3. CHEMISTRY OF SILICA

This chapter introduces briefly the chemistry of silica with the focus on the conditions studied in **Paper 4**, with organosilicates as a silica source in the synthesis of ordered mesostructured silica films. The similarities and differences between the chemistry of silica and titania are discussed and the interaction of the silica precursor and the block-polymer structure directing agent.

3.1 HYDROLYSIS AND CONDENSATION REACTIONS

Synthetic silica is typically prepared using precursors that are either inorganic, such as sodium silicate, or organic silica. The organic silica precursors are typically silicon alkoxides and in this work, tetraethyl orthosilicate (TEOS) was used. In the presence of water the precursor is hydrolyzed as

$$\equiv \mathrm{Si} - \mathrm{OR} + \mathrm{H_2O} \leftrightarrow \equiv \mathrm{Si} - \mathrm{OH} + \mathrm{ROH} \qquad (7)$$

where R is CH_2CH_3 and the horizontal line depict the additional alkoxide groups.[42] The hydrolysis results in the formation of the silanol group Si-OH and exchange of water and ethanol. The hydrolysis can be catalyzed with acid or base, and HCl was used in this work.

The initial step of the condensation reactions is the formation of dimers from the monomers and subsequently oligomers are formed. The oligomers will further grow with time, increasing the amount of siloxane bonds present. The condensation of silica is generally accepted to occur in three stages:

1) Polymerization of monomers to form particles.

2) Growth of particles.
3) Linking of particles into chains, then networks that extend throughout the liquid medium, thickening it to a gel.

The rates in these stages and the type of reactions occurring depend on the conditions in the reaction, where the pH is an important parameter.[49] Varying the pH influences the rate of the reaction, the stability of the formed particles and the density of the formed structures, among other things. In this thesis, the reactions are carried out at pH 2-3. At low pH, between 2 and 7, the condensation rate is assumed to be proportional to the OH^- concentration in the solution and the reaction is divided in two steps.

$$\equiv Si - OH + OH^- \rightarrow \equiv Si - O^- + H_2O \quad (8)$$

$$\equiv Si - O^- + HO - Si \rightarrow \equiv Si - O - Si \equiv + OH^- \quad (9)$$

The first step is the deprotonation of a silanol group. The silanol groups on highly condensed species are more acidic, and are therefore more likely to be deprotonated. This means that monomers preferentially react with larger species than with other monomers. Therefore, once dimers and oligomers are formed, they will continue to grow by the addition of monomers.[42] In this pH range, as the condensation progresses further, particles aggregate into three-dimensional networks and form gels. This may occur through formation of ring-structures due to the strong tendency of silica to form structure that maximize the number of siloxane bonds (Si-O-Si) and minimize the number of SiOH groups. Conversely, in basic solutions, pH 7-10, particles in sol grow in size with decrease in numbers. Under basic conditions, the particles are negatively charged and repel each other. However, the repulsion can be repressed by the presence of salts and aggregation and gelling occurs.[49]

The kinetics of the hydrolysis and condensation of silica precursors are considerably slower than for the equivalent titania precursor. This is due to the partial positive charge of Si in the silica precursor is much lower than on the Ti in the equivalent titania precursor, which makes the silica precursor less susceptible to nucleophilic attack.[42]

4. MESOSTRUCTURED MATERIALS

Today there are a large number of low temperature synthesis methods to produce nanostructured titanium dioxide and silica.[13,50] Nanostructured titania has been prepared in the form of nanoparticles, nanowires, mesoporous materials etc. Mesoporous materials are porous materials with pore size in the range of 2-50 nm according to IUPAC nomenclature. For many applications, having nanostructured materials is a great advantage, partly due to the high surface areas, which provide greater capacity for the material to interact with its surrounding.[51] For semiconductors, such as titania the nanostructure also promotes shorter diffusion paths for excited electrons and holes, which is an important parameter to consider when designing materials for photocatalytic applications or solar cells.[10,13] Moreover, having structures where the pores are ordered, facilitating efficient transport of reactants and products, has been shown to be beneficial for photocatalytic applications.[52]

4.1 STRUCTURE DIRECTING AGENTS

To make porous materials with structural features in the nanometer range, surfactants are commonly used as structure directing agents. Surfactants are molecules that have a hydrophilic polar part, usually called the head, and a hydrophobic non-polar part, typically called the tail. Due to this dual nature of these molecules they tend to aggregate and form so called micelles when introduced into a solution. In an aqueous solution, the hydrophilic part of the surfactant molecule faces the solution, while the hydrophobic parts assemble in the center of the, often spherical shaped, micelle and thereby minimize the interaction with the solution. In a non-polar solvent a reverse micelle is instead formed, where the hydrophobic part faces the solution and the hydrophilic parts are concentrated at the center of the micelle. When the concentration of the surfactants is high, the number of micelles increases and at high enough concentration of the surfactant, the micellar solution will saturate and the mixture goes through a structural

transition and forms ordered structures, so called liquid crystalline phases. There are a number of different phases that can be formed, including cubic phases, hexagonal and reverse hexagonal phases and lamellar phase. Which phase is formed is influenced by several factors, such as the structure of the surfactant, surfactant concentration, temperature and solution composition in a three component system.[53] For phase identification and determination of structure parameters, small angle X-ray scattering is commonly used, discussed in chapter 5.2.3.

In this work, a non-ionic triblock copolymer was used as a structure directing agent. The copolymer consists of a hydrophobic block, poly(propylene oxide) PPO, attached to hydrophilic blocks, poly(ethylene oxide), on each end. The polymer goes under the name Pluronic™ F127 and has the composition $PEO_{100}PPO_{70}PEO_{100}$. A series of Pluronics with various compositions of the hydrophilic and the hydrophobic groups exists and can be used in research and for industrial applications.[54]

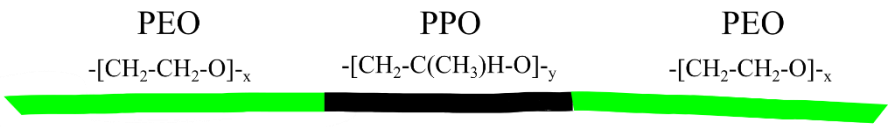

Figure 2. Schematic description of a triblock copolymer. In the Pluronic F127, x=100 and y=70.

The type of structures the Pluronics form in the presence of various solvents and co-solvents has been thoroughly studied.[55–58] For the formation of mesoordered materials, a suitable interaction between the material precursor species and the block copolymer is necessary. For oxides in general, it is agreed that the interaction is mainly between the precursor species and the hydrophilic part of the polymer through hydrogen bonding.[59] In addition, it has been illustrated that other molecular interactions play a role and that the hydrophobic part interacts with the precursor species when the precursor has condensed to a certain degree.[60] The adsorption energy per polymer molecule on, e.g. silica surfaces, has been shown to increase with increasing length of the PEO chains. This was attributed to the increase in number of hydrogen bonds per polymer molecule, showing that the interaction between the PEO chain and the silica species depends on the size of the molecules.[61]

4.2 MESOORDERED TITANIA

The liquid crystalline phases can be used as a template for structuring a variety of materials. In the case of titania, a hydrolyzed titania precursor can be dissolved in the hydrophilic domain of the liquid crystal before it condenses and forms a titania structure replicating the shape of the

hydrophilic domain. Getting the precursor into the hydrophilic domains can be a challenge due to the high viscosity of the liquid crystal phases. One way to bypass this issue is to mix the precursor into a solution with a low surfactant concentration, and lower viscosity, allowing the precursor to mix better with the surfactant molecules. The solvent is then evaporated, inducing co-assembly of the surfactant and the precursor. This generic method was first described by Brinker as evaporation-induced self-assembly (EISA) and demonstrated for silica.[62,63] The solvent evaporation can be achieved with various deposition techniques, discussed in section 5.1.

The template removal is commonly achieved with high temperature treatment or with solvent extraction, leaving a porous mesoordered structure of the metal oxide. The high temperature treatment has the advantage of increasing the crystallinity of the material, which is beneficial for applications such as photocatalysis.[14] However, the temperature needed to remove the template, typically 350-400 °C, disrupts the ordered mesostructure of the mesoporous titania.[15] This is usually attributed to the crystals growing out of the pore walls and into the pores. The solvent extraction method can be carried out at low temperatures, but it usually results in low crystallinity and even solvation of the amorphous titania structure.[16] With the aim of maintaining the ordered mesostructure as well as producing crystalline material there is a large interest in developing low temperature synthesis methods.

4.3 MESOORDERED SILICA

There is a continuous interest in the synthesis of mesoporous silica since its preparation was first reported almost 30 years ago due to the wide-range of applications and its rich chemistry.[18,19,64,65] A large variety of types of geometrical structures, *e.g.* lamellar, hexagonal and cubic, with varying pore sizes and shapes have been prepared using non-ionic Pluronics as structure directing agents.

Studies have suggested that the interaction between PEO and silica occurs only when the silica monomers have condensed to form oligomers of several tens of monomers.[60] It was suggested that it is energetically unfavorable for the PEO chain to lose its hydrated structure to form a few hydrogen bonds with small silica species, but as the silica species grow the number of hydrogen bonds grow making it more energetically favorable to form the hydrogen bonds. Therefore, the degree of condensation of the silica precursor is an important parameter to control when preparing mesoordered silica structures with large molecule block-copolymers as structure directing agent. Low degree of condensation may result in lack of interaction between the

precursor and the polymer and too high degree of condensation may result in lack of mesoorder in the material.[66]

5. EXPERIMENTAL METHODS

The development of films of mesostructured titania and silica was carried out using spray coating. The characterization of the materials prepared in this thesis work was focused on the structure of the material at the atomic scale with X-ray diffraction, X-ray absorption spectroscopy and TEM analysis and on the nanometer scale with small angle X-ray scattering and TEM imaging. In addition, electrochemical methods were used for performance evaluation and electrochemical characterization.

5.1 PREPARATION OF MESOSTRUCTURED FILMS

A central part of the work performed in this thesis was to develop low-temperature spray deposition procedures to prepare ordered mesoporous titania and silica films via evaporation induced self-assembly. With the aim of preparing mesostructured films of titania and silica, a dilute solution of the block copolymer and the silica or titania precursor was spray deposited allowing the solvents to evaporate and increasing the concentration of the block copolymer and the precursor. To form a spray deposited mesoordered film, a suitable solution composition has to be established and several spray deposition parameters have to be regulated, including the nozzle size, the propellant pressure, the distance from nozzle to substrate and the spray duration. In addition, the coating can be applied by continuous spraying or in bursts. These experimental parameters affect the evaporation rates of the solvents and the composition of the deposited film, and therefore have to be tuned to achieve the desired mesoordered film. Other commonly used deposition methods are spin coating and dip coating. The advantages of the spray deposition method is that the film thickness can be controlled, substrates of various shapes and sizes can be used and it is scalable to large surfaces. Both spin coating and dip coating are limited when it comes to the substrate dimensions. In this work the spray deposition was carried out at room temperature so even heat sensitive substrates could be used. The main challenge of

the technique is to reproducibly prepare uniform films. To minimize deviations it is therefore imperative to control the experimental parameters. Additionally, the airbrush and nozzle are cleaned after each use to avoid clogging of the solution pathway. The airbrush used for the spray deposition was an Aztek A470 Airbrush, shown in Figure 3. The airbrush is connected to a gas/air pressure source, the solution is placed in the white sample cup and the pressure is applied using the trigger, driving the solution through the nozzle.

Figure 3. The Aztek A470 Airbrush. The solution is poured in the sample cup and nitrogen was used as the carrier gas. The nozzle used and shown on the picture is a 0.30 mm general purpose nozzle and several types of nozzles are available.

The spray deposition parameters used to prepare the mesoordered titania and silica films are detailed in the following sections.

5.1.1 Spray deposition of mesostructured titania

For the spray deposition in **Paper 2**, the airbrush was placed perpendicular above the substrate and the nozzle-to-substrate was 15 cm. A 0.30 mm general purpose nozzle (Aztek 9305 CX) was used. Nitrogen was used as a carrier gas (1.9 bar) and the flow rate was 2.2 mL/minute. Continuous spraying was applied and the spray time was 15-120 seconds resulting in films of varying thickness. The substrate was glass slides (VWR 631-1551, 76x26 mm). The reaction solution composition was (ethanol:F127:water:HCl:titanium butoxide) (65:0.18:69:6.9:4.4) mmol, a composition that was adopted from earlier work on spin-coated titania films.[67]

5.1.2 Spin coating of mesostructured titania

For comparison, spin coated films were also prepared from the same solution composition. A glass slide is placed on a spinner and the precursor solution (7 drops, 0.14 g) is dropped onto the glass slide and while it was spun at 300 rpm for 5 seconds, followed by 1000 rpm for 10 seconds in a spinner (SPIN150 wafer spinner APT GmbH). The advantage of spin coating is that it is convenient and reproducible. The disadvantages are that the the film coverage is not

evenly distributed over the whole substrate and, due to the need to spin the substrate at high speed, scaling up is an enormous challenge.

5.1.3 Spray deposition of mesostructured silica

The experimental setup for the spray deposition of silica in **Paper 4** was identical to the titania deposition setup. The films were deposited directly on mica sheets (XENOCS 10 mm diameter, 5-7 µm thickness) for SAXS measurements or on glass slides for calcination. By optimizing the solution composition and the spray procedure we found that 40 rounds of 0.5 seconds spray and 0.5 seconds pause between spray bursts resulted in mesoordered films. Attempts to perform continuous spraying with the solution resulted in insufficient evaporation of the solvents, leading to formation of a liquid coating that appeared not to contain any order on the mesoscale.

5.2 Structural characterization techniques

5.2.1 X-ray diffraction

X-ray diffraction is one of the most commonly used analysis techniques for crystalline materials. It is a versatile technique that can be used to identify crystal structures, determine the phase purity and the crystallite size and shape in a material. In short, when a monochromatic X-ray beam is irradiated on to a sample, a part of the X-rays will be scattered and if the sample is crystalline, the X-rays will be partly diffracted at certain angles. Figure 4 illustrates when the condition for constructive interference is fulfilled and X-ray diffraction occurs.[68]

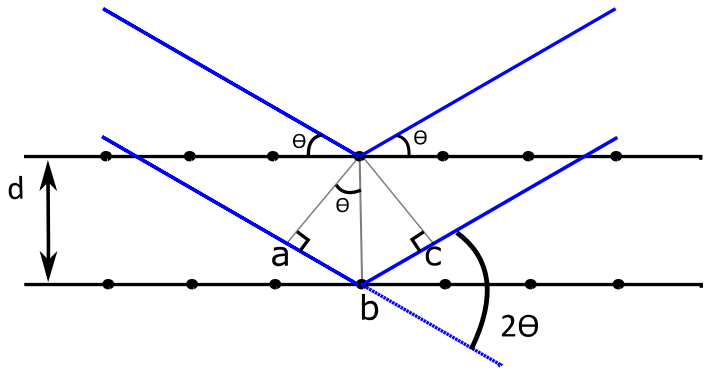

Figure 4. Graphical description of the Bragg equation.

The monochromatic X-ray beam meets the crystal planes of atoms at an angle Θ. A part of the beam is scattered on the first layer, and a part of the beam is scattered on the layer below. For

the scattered beams to arrive in phase with each other, the difference in path lengths must be an integral number of the wavelength. In Figure 4, the difference in path length is $ab + bc$, and since $ab = bc = d * \sin\theta$, the difference in path length can be written as $2d * \sin\theta$. If the X-ray wavelength is λ, Bragg's law is fulfilled when

$$n\lambda = 2d\ sin\ \theta \qquad (10)$$

A detector is used to measure the intensity of the outgoing diffracted beam and a diffraction pattern can be constructed by varying the angle between the incident beam, the sample and the detector. The diffraction pattern is usually given as scattering intensity as a function of the scattering angle, 2Θ. The diffraction occurs as so called Bragg peaks at angles which are specific to each crystal structure and they can thus give structural information of the measured sample. XRD is commonly used as a fingerprint method to detect a known structure in a sample, where the measured pattern is compared with a database of known structures. In that way it is a quick and useful method to analyze qualitatively which phases are present in the measured sample. It is mainly the positions and the intensities of the peaks that reveal the crystalline phases present in a sample, but the shape and width of the peaks contain important information as well.

The width of the diffraction peak increases with decreasing crystallite size. When the measured angle, 2Θ, deviates from the Bragg angle, the diffracted beam will destructively interfere resulting in a sharp peak. This is achieved with a diffraction of the beam on a large number of planes, but as the crystallite size decreases the number of planes also decreases resulting in incomplete destructive interferences around the Bragg angle and a broader peak is observed in the diffraction pattern. The mean crystallite size, τ, can be calculated from the peak broadening with the Debye-Scherrer formula:

$$\tau = \frac{K\lambda}{\beta \cos\theta} \qquad (11)$$

where λ is the photon wavelength, K is the shape factor, β is the full width at half maximum of the peak (FWHM) and θ is the Bragg angle.[68]

To determine the weight fraction of the amorphous phase and the crystalline phases, measurements with diamond as an internal standard were carried out. A small, known amount

of diamond was added to the each sample and the XRD pattern was measured. Diamond was selected because it is highly crystalline and none of the major peaks of rutile, anatase or brookite overlap with the diamond peaks. Using Rietveld analysis, the fraction of diamond and rutile was determined. The absolute weight fraction of rutile was then calculated

$$W_{abs(rutile)} = W_{meas(rutile)} * \frac{W_{std(known)}}{W_{std(meas)}} \quad (12)$$

where $W_{meas(rutile)}$ is the weight fraction of rutile, determined by Rietveld analysis of the diffractrogram, in the sample containing the diamond, $W_{std(known)}$ is the weight fraction of the diamond added in the sample and $W_{std(meas)}$ is the weight fraction of the diamond in the sample determined from Rietveld analysis of the XRD diffractogram. The relative weight fractions of rutile, brookite and anatase, determined from the pure samples (w/o diamond), were used to determine the absolute concentrations of these phases.

$$W_{abs(brookite)} = W_{relative(brookite)} * \frac{W_{abs(rutile)}}{W_{relative(rutile)}} \quad (13)$$

where $W_{relative(brookite)}$ and $W_{relative(rutile)}$ is the relative fraction of the phases determined from the sample without any internal standard diamond. The absolute concentration of anatase was determined in the same way. The concentration of the amorphous phase was calculated

$$W_{abs(amorph.)} = 1 - \left(W_{abs(rutile)} + W_{abs(brookite)} + W_{abs(anatase)}\right) \quad (14)$$

The total crystallinity is the sum of the absolute concentrations of rutile, brookite and anatase.

5.2.2 RIETVELD REFINEMENT

Rietveld refinement analysis was used to analyze quantitatively the phase composition from a diffraction pattern. The method allows for quantification of phases, even when the phases have overlapping peaks. First, a trial structure is created by the user and a diffraction pattern is calculated. The calculated pattern is then compared with a measured pattern and by applying the Rietveld method the trial structure parameters are refined and the overall profile difference between the calculated pattern and the experimental pattern is minimized. The method was first described by Hugo Rietveld and although the method was first developed for neutron

diffraction, it has been successfully used for X-ray diffraction as was suggested in the original papers.[69,70]

In this work the Fullprof software was used to perform Rietveld analysis to get quantitative information about the polymorph distribution in titanium dioxide nanomaterials.[71] There were three polymorphs considered in the refinements, rutile, anatase and brookite. When performing the refinements it is of high importance to start from the trial structures that are representative of the phases being analyzed. The structures for the three phases are given in the ICDD database and the site occupancies, positions and atomic displacement parameters were fixed to literature values.[72,73] The Instrumental Resolution Function (IRF) was determined by collecting a PXRD pattern of a LaB_6 NIST 660A standard under identical conditions as the synthesized samples and refining the profile parameters to describe the instrument in the best possible manner. When starting the refinement of the samples, one must consider in which order to refine the parameters. In the work presented, first the background was described by a four coefficient Chebyshev polynomial function. Then the zero, which accounts for shifts of peaks, was refined. The intensity of the peaks, the scale, was then refined. However, in some cases refining the scale may result in much lower calculated intensities of the peaks than the measured pattern. In that case, one should fix the scale so that the peaks in the calculated pattern become approximately the same size as the measured one and refine the scale later. The unit cell parameters were then refined. Subsequently, the Lorentzian size broadening, which gives information on the crystal size, was refined. In many cases the Lorentzian size refinement contributed to a better fit, but did not give satisfactory results. Attempts were made to describe the remaining misfit by refining the strain, but that did not improve the fit and was therefore not used. To model the size broadening anisotropically, a linear combination of maximum 4 spherical harmonic functions was used. This was done for all three phases. Since the relative amount of brookite in some samples was much higher than originally expected, an attempt was made to first refine all of the above for only the rutile and the anatase phase before including brookite phase but that did not affect the relative amount of brookite.

5.2.3 Small angle X-ray scattering

SAXS is an analytical method which is used to characterize the structure of materials on the nanometer scale. The method is typically used to resolve structures in the range of 1-100 nm, but the range can be extended in both directions with certain experimental setups. This is about the same dimensions as are characterized with electron microscopy, but the investigated sample volume is much larger so the data contains averaged information from the sample making the

techniques complementary to each other. In a SAXS measurement, a sample is exposed to a monochromatic X-ray beam and the scattering pattern of the beam at small angles is measured with a 2D detector behind the sample. The radially integrated intensity of the scattered beam is typically plotted as a function of the scattering vector transfer or scattering q, which is related to the scattering angle Θ as

$$q = \frac{4\pi \sin\theta}{\lambda} \qquad (15)$$

In ordered mesostructured materials the SAXS peak pattern can be used to determine the type of mesostructure obtained and the peak positions contain information about the dimensions of the structure.[74]

In **Paper 2**, mesoporous titania samples were scraped of the glass substrate, gently ground in a mortar and placed in a quartz capillary (1.5 mm outer diameter, Hilgenberg) and measured for 450 seconds under vacuum. In **Paper 4**, prior to calcination, the deposited mesoordered silica was measured on mica sheet. Briefly, the synthesis solution was spray deposited on a mica sheet and a sandwich cell was assembled with two mica sheets, one blank and one spray coated on one side, facing each other with a rubber O-ring between them. The whole cell was held together by two stainless steel discs with holes in the center. Within a few minutes of assembling the sandwich cell, the SAXS measurement was started and data was collected for 30 minutes. When assembled, the mica sheet with the spray deposited coating was placed closer to the detector with the coating facing the rubber ring, so that the sample was isolated from the vacuum of the sample chamber. After calcination, mesoporous silica films were scraped of the glass substrate and measured in a quartz capillary. SAXS measurements were performed in a Mat:Nordic SAXS/WAXS/GISAXS instrument from SAXSLAB.

5.2.4 X-RAY ABSORPTION SPECTROSCOPY

The local atomic structure of the titanium atoms was investigated by X-ray absorption spectroscopy (XAS). High energy X-rays with tunable wavelength are used to scan the spectrum in proximity of the absorption edge of the selected element. The absorption edge is observed by an abrupt increase in the X-ray absorption, which occurs when the energy of the incoming X-ray beam matches the energy needed to excite a core electron to the vacuum. The K-edge of the titanium atom was measured, which is at 4.996 keV for a reference titanium foil where the oxidation state of titanium is 0. The edge position is affected by the oxidation state

of the measured element, where a higher oxidation state shifts the absorption edge to higher energies.

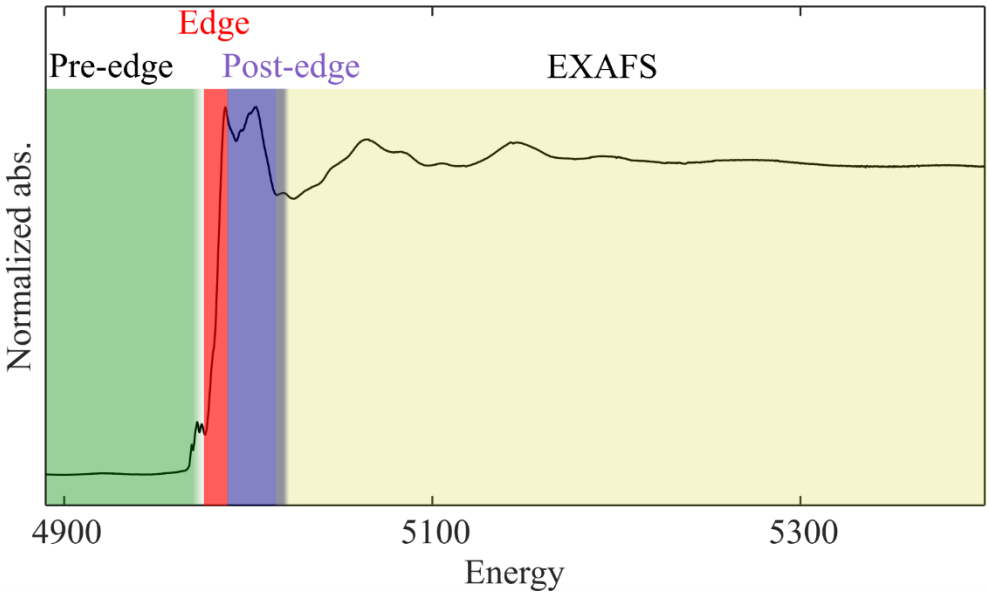

Figure 5. Titanium K-edge absorption spectrum of anatase, showing the pre-edge, the edge, the post-edge and the EXAFS regions.

The region around the absorption edge is typically divided in four regions; the pre-edge region, the edge region, the near edge region and the extended X-ray absorption fine structure (EXAFS), depicted in Figure 5. The titanium pre-edge contains several peaks which have been attributed to electronic transitions of the 1s electrons to the outer orbitals. The relative intensities and the positions of these peaks were used to determine the coordination number of the titanium atom in the mesoporous titania.[75–77] The absorption edge position was used to determine the oxidation state of the titanium atom in the samples. It has been observed that the edge shift is 3 eV between Ti^{4+} (TiO_2) and Ti^{3+} (Ti_2O_3).[78] The near edge X-ray absorption fine structure region (NEXAFS) extends from a few eV to about 50 eV above the edge. The spectral features in this region are attributed to scattering of ejected photoelectrons with the atoms of the first shell around the absorber. Additionally, relatively long scattering pathways involving tightly bonded atoms beyond the first shell can give significant contributions.[79,80] The EXAFS region contains contributions from backscattered photoelectrons of high kinetic energy and is characterized by weak oscillations of low frequency. X-ray absorption measurements were performed at the Balder XAS beamline of the MAX IV synchrotron in Lund, Sweden.[81] The

measurements were carried out in transmission mode and titanium foil was used as a reference for energy calibration of the spectra.

5.2.5 TRANSMISSION ELECTRON MICROSCOPY

Transmission electron microscopy is a high-resolution technique used to image and characterize materials on the nanometer and the atomic scale. The size and shape of particles can be observed as well as the crystal structure of materials can be determined. High energy electrons, typically >100 kV, are accelerated through a sample and an image is generated from the transmitted electrons. The electrons have a very short wavelength, which makes it possible to reach high resolution of about 0.1 nm in modern instruments. Because electrons have to travel through the sample to generate an image, the sample has to be very thin and the general recommendation is less than 100 nm thickness. TEM has two basic operating modes, bright field imaging mode and dark field diffraction mode. In the bright field mode, an image is generated based on the transmitted electrons where a thick area of the sample appears dark and areas with no sample or thinner sample appear light. In dark field mode the direct beam is blocked but the diffracted beam appears bright. In this mode it is therefore possible to capture electron diffractograms, usually called selected area electron diffraction (SAED).

TEM was used to evaluate the size and shape of the titania particles and SAED was used to determine the crystal structure in **Paper 1**. In **Papers 2** and **4**, TEM was used to visualize and evaluate the ordered mesostructure in the titania films as well as measure the pore size, crystal size and determine the crystal structure. The samples were prepared by grinding and dispersing in ethanol. 1-2 drops of the dispersion were then dropped onto a lacey carbon coated copper grid and the ethanol was evaporated. The experiments were performed on a FEI Tecnai G2 microscope, operating at 200kV.

In **Paper 3**, the TEM samples were prepared by a TEM lamella lift-out technique in a FIB/SEM. The lamella was attached to a copper half grid and was ion thinned to transparency in the FIB/SEM. The TEM observations were performed on a FEI Tecnai G2 operating at 200 kV and elemental maps were produced by energy filtered (EF) TEM experiments, performed on a FEI Titan operating at 300 kV.

Energy filtered experiments are based on the inelastic scattering of some of the electrons from the high energy electron beam. The transmitted electrons are directed into a magnetic spectrometer which deflects the electrons according to their kinetic energy, producing an electron energy-loss spectrum (EELS) and energy filters are used to pass electrons of a selected energy interval through, to form the image. The energy loss of the inelastic scattered electrons

is characteristic of the element it interacts with. The background was subtracted using a 3 window method, where the background is obtained by measuring two windows at energies just below the absorption edge, as depicted in Figure 6.[82] In our work, the areas were energy filtered to generate C, Li, Ti and O elemental maps.

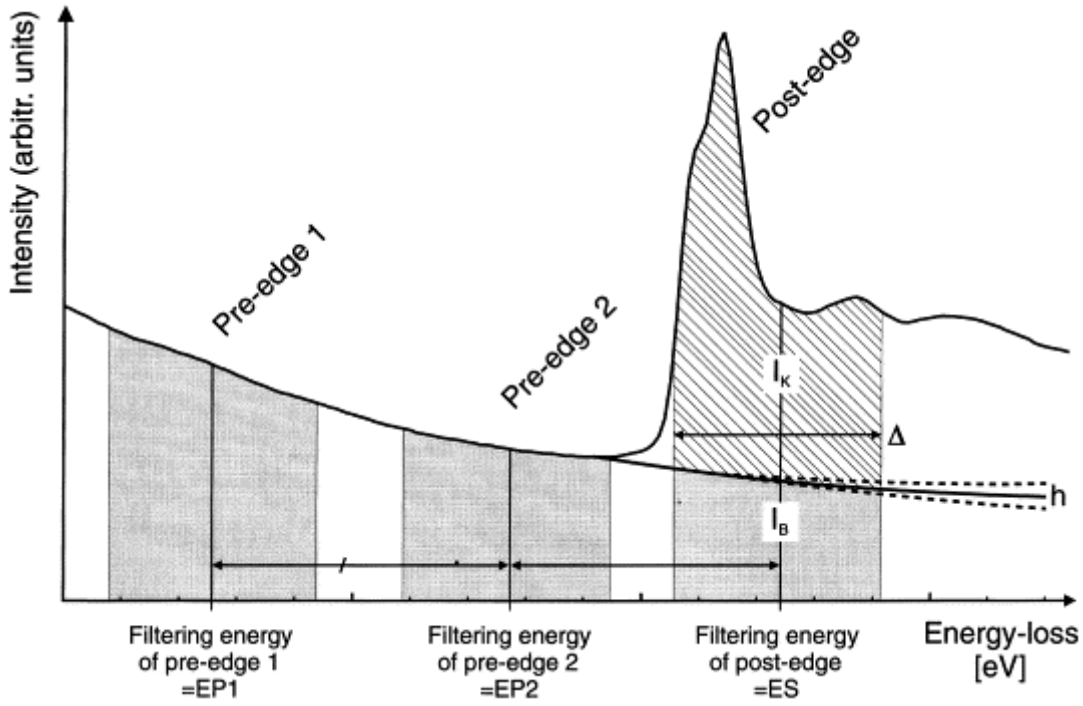

Figure 6. Schematic representation of the three window method. The background is estimated from pre-edge 1 and 2 and subtracted from the post-edge image. Reproduced from reference [82].

5.2.6 PROFILOMETER

KLA Tencor D100 profilometer was used to measure the thickness of the deposited films. A sharp object was used to scrape a sharp line of the sample from the substrate. Subsequently, the surface is scanned perpendicular to the line with a sensor. The force applied was 0.03 mg and the scan speed was set 0.07 mm sec^{-1}.

5.3 ELECTROCHEMICAL TECHNIQUES

Electrochemical techniques were used to study the viability of using mesoporous titania as anode material in lithium ion batteries in **Paper 3**. Chronopotentiometry and cyclic voltammetry measurements give insight to the charge and discharge behavior, including the specific capacity, the capacity retention and the voltage onset of the irreversible capacity.

5.3.1 ELECTRODE AND ELECTROCHEMICAL CELL CONFIGURATION

The electrochemical performance of the electrode is affected by the properties of the active material and by the preparation of the electrode and assembly of the electrochemical cell. Therefore, it is imperative that the electrode preparation procedure and the assembly of the electrochemical cell is reproducible to compare the active materials in a reliable way. Titania is a poor electrical conductor and was mixed with carbon to increase the conductivity of the electrode and binder was added to increase the adhesion of the mixture to the copper current collector. The electrode preparation procedure is as follows; titania, mesoporous or anatase nanoparticles, and carbon black Super-P™ were mixed by ball milling at 10 Hz for 10 minutes in weight ratio (8:1) (titania:carbon). The ball milled mixture was transferred to a glass vial and Kynar® 5% (w/w) in NMP was added and the mixture was stirred overnight in a capped vial, forming a slurry. The weight ratio of (titania:carbon:dry PVDF) was (8:1:1). The slurry was poured onto copper foil placed on a motorized automatic film applicator. A stainless-steel doctor blade was used to coat a 150 µm thick coating of the wet slurry. The coating was let dry overnight at room temperature with additional drying at 80 °C for 2 hours. For preparation of electrochemical cells, electrodes were cut in 10 mm diameter circular pieces of the coated copper foil and dried in a high vacuum oven at 70 °C for 2 hours before being transferred to a glove box. The cells were assembled in the glove box under argon atmosphere with oxygen and water content less than 1 ppm.

For chronopotentiometry measurements, coin cells were prepared with the electrode as a cathode and a lithium disc as an anode, shown in Figure 7a. The titania/carbon electrode was placed in a coin cell case with casing and wet with 20 µL of the electrolyte (LP30). A glass microfiber separator was used and further 40 µL LP30 was used to soak the separator. Lithium disc was pressed to the spacer and placed on top of the separator, with the lithium disc facing the separator. A spring was placed on top of the spacer and the cell was sealed by pressing the cell with a cap.

Cyclic Voltammetry (CV) measurements were performed with a three electrode T-cell setup, shown in Figure 7b. The working electrode (WE) and the counter electrode (CE) were pressed together with a separator between them. The cell was filled to the brim with electrolyte before the reference electrode (RE) inserted was above the WE and CE. Lithium discs were used as CE and RE. The cell was closed and sealed with Parafilm ® laboratory film and aluminum foil to prevent leaking and evaporation of the electrolyte out of the cell and oxygen/moisture from entering the cell.

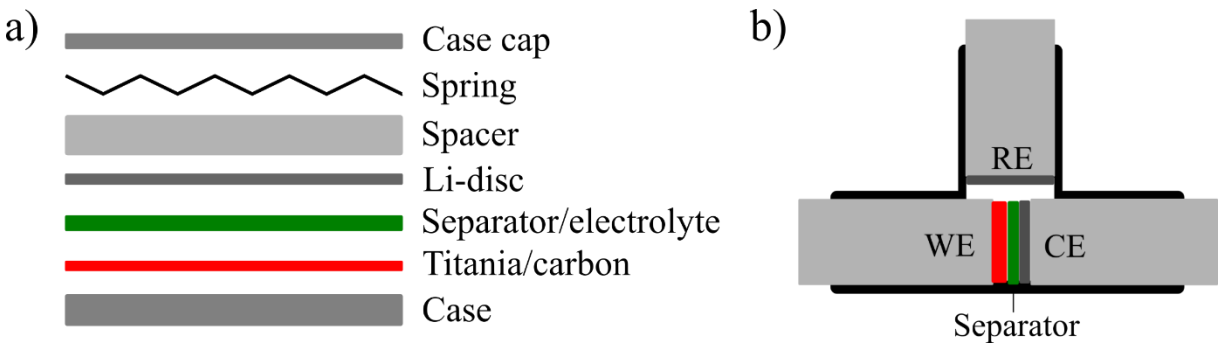

Figure 7. Coin cell configuration (a) and CV configuration (b). Titania electrode (WE) is red, the separator is green and the lithium discs (CE and RE) are dark grey. In (b) the outer layer is made from inert, electrically insulating material.

5.3.2 CHRONOPOTENTIOMETRY

Chronopotentiometry is a technique where a controlled, typically constant, current is applied between the WE and the RE and the potential is recorded. In a two electrode setup, the same electrode serves as the CE and RE. In **paper 3** the performance of mesoporous titania electrodes was evaluated in a two-electrode half-cell configuration with lithium foil as CE/RE, shown in Figure 7a. In cyclic chronopotentiometry, the applied current direction is alternated between charge and discharge as the recorded potential reaches the defined charge/discharge cut-off potential.[83] The current is expressed in C rates, which is a multiple of the theoretical capacity of lithium intercalation into the anatase phase of titania, 335 mAh g^{-1}.[84] For example, 1 C and 0.5 C equal currents of 335 mA g^{-1} and 167.5 mA g^{-1} of mass of titania, respectively. The technique provides a way to evaluate the specific capacity, the capacity retention during cycling, the rate capability and the charge/discharge behavior of the measured electrode. The chronopotentiometry measurements were carried out with a Scribner 580 battery cycler, between 0.7 V and 2.9 V at the current rate 165 mA g^{-1} (0.5 C), and rate capability tests were performed at current rates from 1 C to 100 C.

5.3.3 CYCLIC VOLTAMMETRY

Cyclic voltammetry was carried out by scanning the potential between two defined potential limits and record the current. Once the defined potential limit is reached, the direction of the scan is switched and the potential is scanned until the other potential limit is reached. CV measurements were carried out at voltages from 0.7, 1.0, 1.3, or 1.7 to 2.9 V, respectively, with scan rate 0.3 mV s^{-1} and cycled for 50 cycles. The potential limits were selected to include discharge peaks observed in the first scan to 0.7 V. The measurements were used to study the lithium intercalation processes and the onset of the irreversible processes, observed by the

chronopotentiometry measurements. The lithium concentration in the electrodes was deducted from the CV reduction curves by calculating the specific capacity from the current response over time

$$C = \int I dt \tag{16}$$

Where I is the measured current and t is the time. For the scans that were interrupted in the deintercalated state, the lithium remaining in the electrode was calculated as the difference in specific capacity of the first and fiftieth cycle. For the scan interrupted in the intercalated state, the lithium concentration was calculated as the specific capacity of the first reduction curve. The measurements were carried out with a Bio-Logic VMP-3 potentiostat in a 3 electrode T-cell configuration, where lithium discs were used as the WE and CE. The data is presented as a plot of current density vs. potential.

6. POLYMORPH SELECTIVITY

In **Paper 1**, we investigated the influence of synthesis time and titania precursor concentration on the polymorph selectivity of titanium dioxide nanoparticles in an acidic and low-temperature synthesis. As the reaction progresses, and titania particles are formed, the chemical composition of the synthesis mixture changes and the effect of the composition evolution on the polymorph selectivity was investigated.

Three series with different initial titania precursor (titanium butoxide) concentrations were studied and samples with synthesis times between 3 to 56 days were prepared from each series. In short, ethanol and 5 M HCl were mixed in a 20-mL glass vial and titanium n-butoxide was added to the solution before the vial was capped and the content shaken until the mixture became clear. The vial was placed in an oven, heated to 40 °C. After the desired synthesis time, the sample mixture was removed and the formed titania particles were retrieved and washed three times with ethanol centrifugation at 20000 rpm for one hour in a Beckman Coulter Ultracentrifuge Optima 100XL with a Type 90 Ti fixed angle rotor (25000 x g). The particles were dried at 40 °C. The initial solution composition of the three series is listed in Table 1 and the synthesis time of each sample is shown in Table 2.

Table 1. Solution composition in series A, B and C.

Series	Ethanol [g]	5 M HCl [g]	Ti-butoxide [g]
Series A	3	1.5	1.5
Series B	3.6	1.5	0.75
Series C	2.1	1.5	2.6

Table 2. Synthesis time of samples in series A, B and C.

Synthesis time [days]	3	5	7	11	14	24	32	39	56
[Ti] = 0.65 M	A1	A2	A3	A4	A5	A6	A7	A8	A9
[Ti] = 0.33 M			B1		B2		B3		B4
[Ti] = 1.12 M			C1		C2		C3		C4

XRD measurements and Rietveld refinements were performed on all samples to evaluate the influence of titania precursor concentration and synthesis time on the polymorph selectivity. Rietveld refinement (described in chapter 5.2) was used for phase quantification in each sample. Figure 8a shows the XRD patterns of the samples in series A. The diffractograms clearly show that at short synthesis times the samples are mostly composed of the rutile polymorph and with increasing synthesis time the fraction of the brookite and the anatase polymorphs increases. Figure 8b shows the refinement of sample A5.

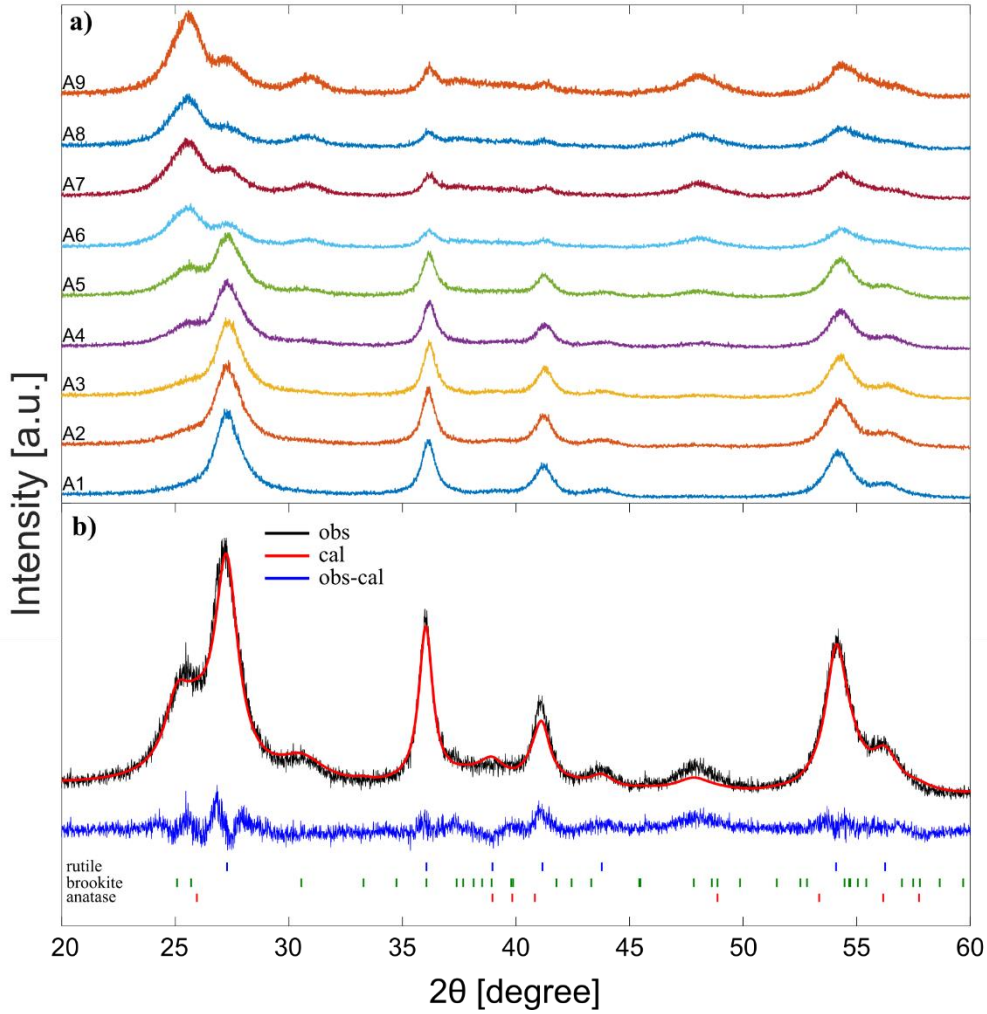

Figure 8. a) X-ray diffractograms of samples A1-A9. The diffractograms are in the order of increasing reaction time, from bottom to top and off-set in intensity for clarity. b) Rietveld refinement of sample A5. The observed pattern is shown in black, calculated pattern in red and the difference between observed and calculated is shown below in blue. The Bragg peak positions for each phase are indicated below. Reproduced from reference.[44]

Quantification of the phases was achieved with Rietveld refinements of the diffractograms of the samples in all three series. Figure 9 shows the relative weight fraction of the polymorphs in series A (a), series B (c) and series C (e). In all three series the relative weight fraction of rutile

is initially high, about 50-80% after 7 days synthesis time but the fraction of brookite and anatase increases with increasing synthesis time and after 56 days the fraction of brookite is about 60 and 70 % in series A and B, respectively. Comparing the three series, increasing initial titania precursor concentration results in higher fraction of rutile polymorph.

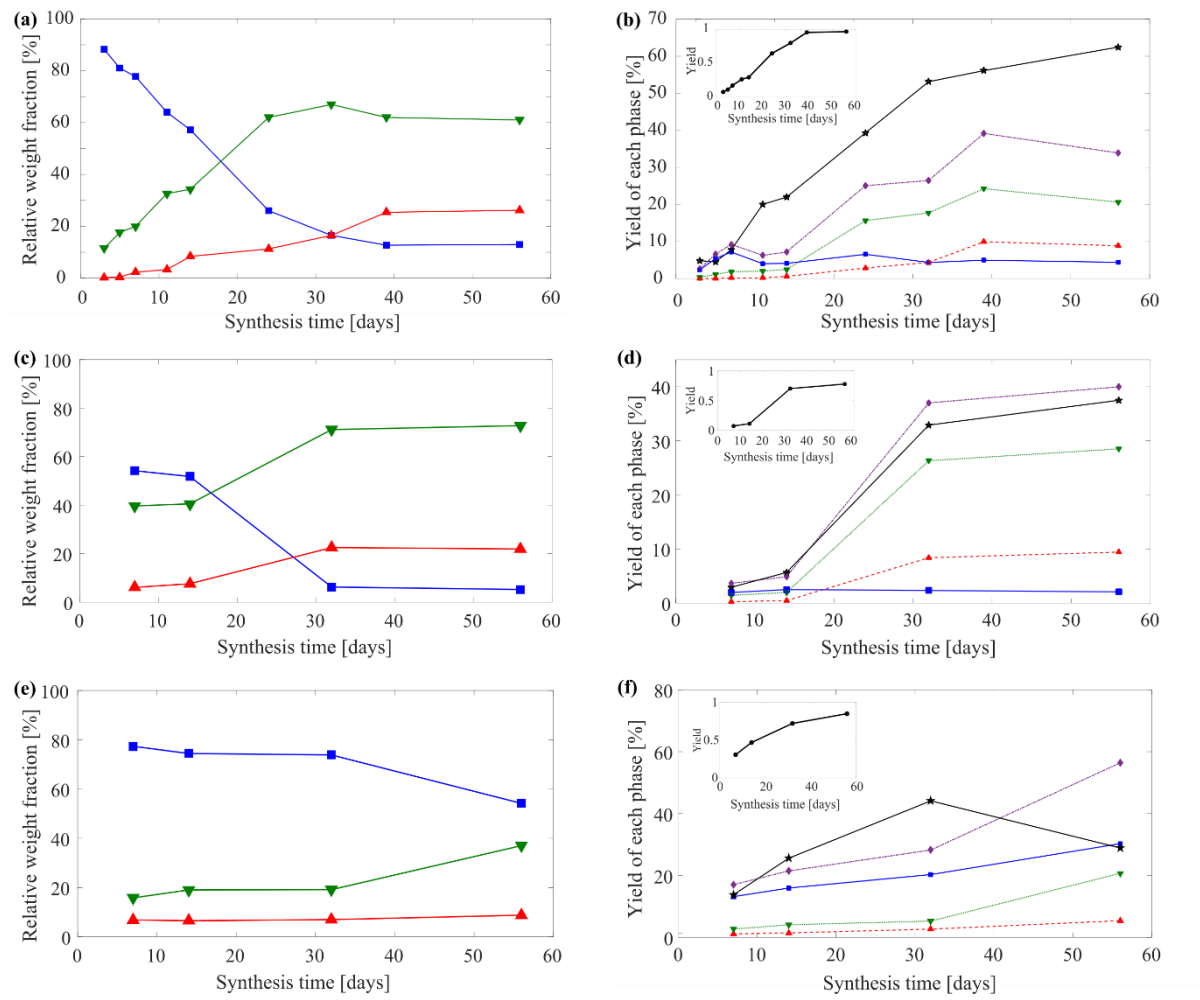

Figure 9. Relative weight fraction of the polymorphs and the yield of each phase for series A (a,b), series B (c,d) and series C (e,f). In all graphs the phases are represented by the following symbols: rutile (blue squares), brookite (green down-pointing triangles), anatase (red up-pointing triangles), total crystallinity (purple diamonds) and amorphous phase (black stars). The insets in (b,d,f) show the reaction yield. Reproduced from reference.[44]

The total amount formed of each phase is displayed in Figure 9 for series A (b), series B (d) and series C (f). The yield of each phase is the product of the weight fraction and the total yield of the reaction. In addition, to determine the yield of the rutile, anatase and brookite polymorphs, the total crystallinity of the material was assessed by performing XRD measurements with an internal measurement standard. In series A, mainly rutile is formed in the first 7 days and from 11 days onwards the absolute amount of rutile formed remains nearly constant. From 14 days and onwards, mainly brookite and anatase are formed. In series B, with

about half of the initial precursor concentration in series A, a similar trend is observed where rutile is formed during the first 14 days after which the yield of rutile remains nearly constant, but the yield of the phase is notably lower than in series A. After 14 days mainly brookite and anatase are formed. In these two series, the yield of the rutile phase does not decrease while we observe a large formation of brookite and anatase crystal structures, suggesting the two phases are not formed via transformation of the rutile crystals but that they crystallize separately at the later stages of the reaction. In series C, mainly rutile had formed after 7 days and it continued to form during the whole synthesis time. Minor amounts of anatase and brookite are formed until 32 days, but between day 32 and 56 more brookite is formed. In all three series there is a change in polymorph selectivity with synthesis time.

The shape of the crystallites was predicted from the Rietveld analysis of the XRD patterns and imaged with HR-TEM images. Figure 10 shows HR-TEM image (a) and the shape predicted from the Rietveld analysis of the diffractogram (b) of the rutile crystallites in sample A1. The d-spacing and indexing of the FFT confirms the presence of the rutile polymorph. The XRD measurements and TEM analysis are in excellent agreement, showing needle shaped crystals of about 10 nm in length.

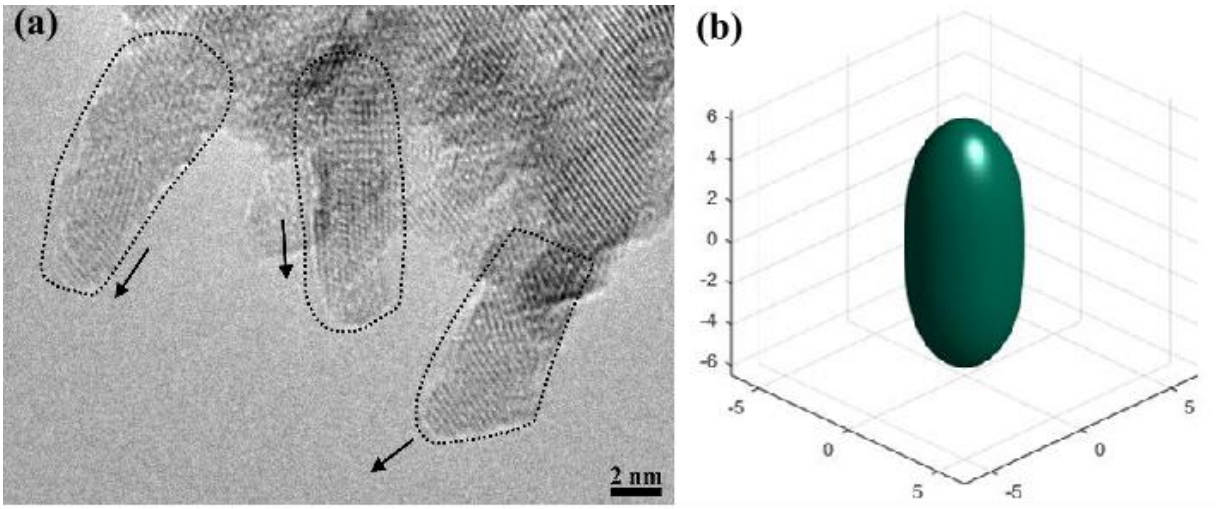

Figure 10. HR-TEM image of sample A1 (a) and predicted size and shape of rutile crystals from diffraction pattern and Rietveld analysis (b). The axes units are nm in (b).

Figure 11 shows a HR-TEM micrograph (a) and the shape predicted from the Rietveld analysis of the diffractogram (b) of the brookite crystallites in sample A9. The Rietveld analysis shows an oblate spheroid shaped crystal, and the TEM analysis shows a 2d circular shaped crystal of a similar size. SAED confirmed the presence of the brookite polymorph of the sample (shown in **Paper 1**).

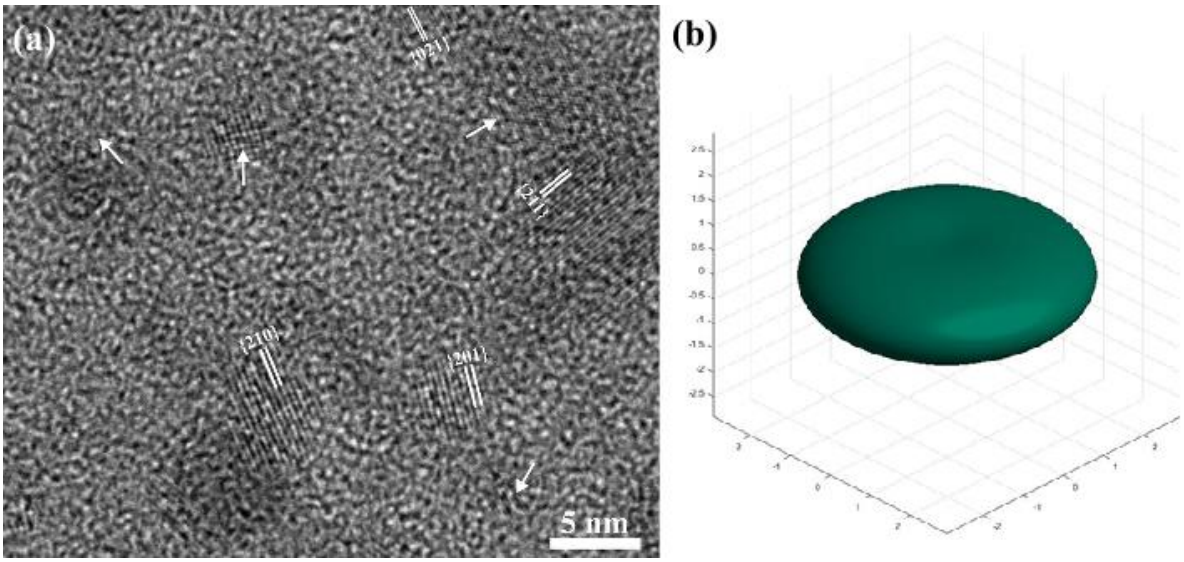

Figure 11. HR-TEM image of sample A9 (a) and predicted size and shape of brookite crystals from diffraction pattern and Rietveld analysis (b). SAED and d-spacing measurements confirmed that brookite is the main phase in the sample. The axes units are nm in (b).

The results show that in the low temperature and low pH system studied, rutile is primarily formed during the initial stages of the reaction, whereas anatase and brookite fractions increase with synthesis time. It is confirmed that a solid-solid transformation or a dissolution-crystallization transformation process of rutile to anatase or brookite is improbable under these synthesis conditions. The formation of anatase and brookite instead occurs through condensation of unreacted titania precursor in the solution and the time dependent polymorph selectivity is instead related to changes in the chemical environment of the system, where rutile is mainly formed at high precursor concentrations but anatase and brookite are selectively formed as the concentration of the precursor decreases.

7. SYNTHESIS OF MESOPOROUS TITANIA FILMS

A low temperature synthesis method for preparation of mesoporous titania is described in **Paper 2** and the deposition methods are detailed in chapter 5.1. The synthesis procedure is delicate, and several synthesis parameters have to be carefully controlled to obtain ordered mesoporous titania films. In previous studies performed by our group,[67,85–87] the films were deposited by spin coating the solution, which is a convenient and reliable method but difficult to scale up, due to inherent size limitation of spinning a substrate at high speed. Moreover, spin coating results in an uneven film distribution over the substrate. To further develop the synthesis, we studied a new scalable spray deposition method which makes it possible to deposit films quickly and evenly on large substrates. The spray deposited films' morphology and crystal structure were characterized and compared to films produced with the already established spin-coating deposition. Additionally, the influence of synthesis time before deposition, aging time after deposition and film thickness on the atomic order and the mesostructure of the films were evaluated.

In short, the reaction solutions were prepared by stirring 2.25 g Pluronic™ F-127 triblock copolymer ($PEO_{100}PPO_{70}PEO_{100}$), 3g ethanol and 1.5 g 5 M HCl in a polypropylene bottle at room temperature until the polymer was completely dissolved. At that stage, 1.5 g titanium butoxide was added to the solution and stirred until the precursor was completely dissolved. The molar composition in the reaction solution was (Ethanol:F127:water:HCl:titanium butoxide) (65:0.18:69:6.9:4.4) mmol. The solution was heated to 40 °C in a closed vessel and stored for 3-24 hours. Subsequently, the solution was spray deposited or spin coated onto a glass slide.

In **Paper 2**, a low temperature synthesis method was developed from the synthesis reported by Nilsson et al.[67] to prepare polycrystalline hexagonally ordered mesoporous titania. The four

synthesis steps of the new method are illustrated graphically in Figure 12 and are summarized in four steps:

i) Condensation and nucleation of titania in a reverse microemulsion.

ii) Spray deposition, solvent is evaporated inducing the formation of liquid crystal phase, with the titania species in the hydrophilic domains.

iii) Aging, where the titania species further condensate and crystallize at high relative humidity.

iv) Removal of the surfactant template by UV treatment.

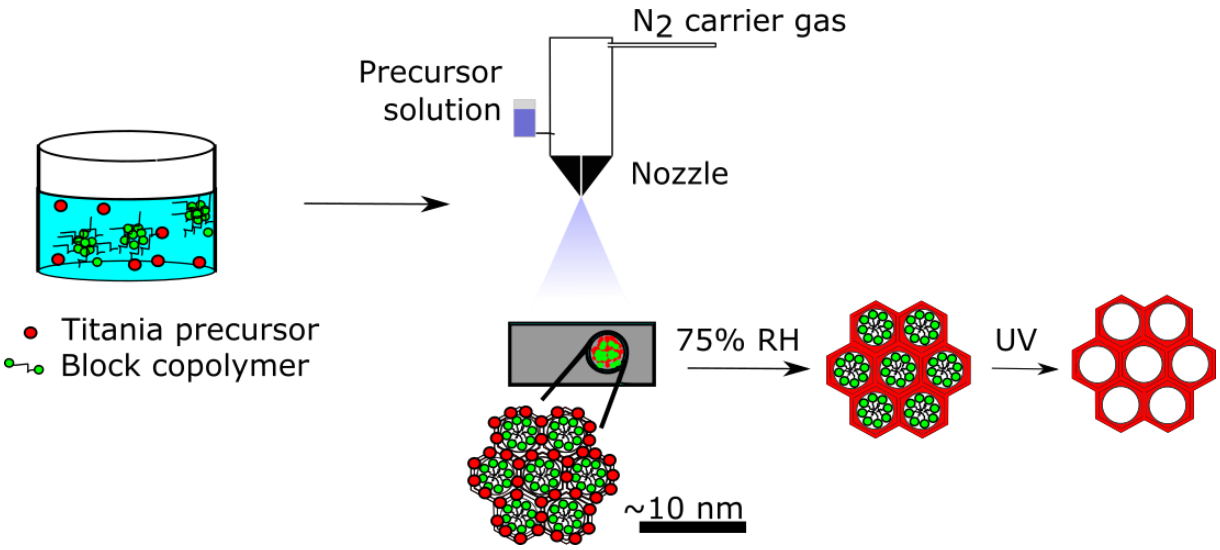

Figure 12. Graphic scheme of the synthesis of mesoporous titania using spray coating. i) The titania precursor hydrolyzes and condensates in the hydrophilic domains of the reverse micellar solution. ii) Solvent evaporates and solution is deposited onto a glass slide, increasing the concentration of the surfactant and leading to formation of hexagonal liquid crystalline phase with titania species integrated in the hydrophilic regions. iii) The titania species further condensate and crystallize at high relative humidity. iv) The surfactant template is removed with UV treatment.

The deposited films were stored at high relative humidity for 1-120 hours before the template was removed with UV treatment for 24 hours. To characterize the overall mesoorder of the films, Small Angle X-ray Scattering (SAXS) was employed. Conventional and high-resolution Transmission Electron Microscopy (HR-TEM) techniques were used for the morphological and microstructural characterization of the material.

7.1 THE EFFECT OF THE DEPOSITION METHOD ON THE MESOSTRUCTURE

To study the influence of the deposition technique on the mesostructure, films were prepared with spin-coating and spray-coating. Polycrystalline hexagonally ordered mesoporous titania thin films were prepared by spin-coating on glass substrates in previous studies performed in our research group.[67,85–87] The hexagonal mesostructure was achieved via evaporation of the solvents during the spin coating (EISA method). However, when spray deposited, the solvents evaporate at different rates and it is imperative to establish a combination of solution composition that is suitable for spray deposition and a spray deposition procedure which is compatible with the solution. The solution composition that was previously used to prepare spin-coated films was initially tested to make spray-coated film. The resulting films were characterized with SAXS and TEM imaging and compared with the spin-coated film. Figure 13 shows the SAXS patterns of samples produced by the spray-coating and the spin-coating technique before template removal (a) and after template removal (b), (c)-(f) are discussed later. For samples shown in (a,b) the reverse micellar solution was heated to 40 °C for 3 hours before deposition, and aged for 72 hours after deposition. The spray coated films were prepared by 15 seconds continuous spraying. Before and after the template removal, the patterns of the spin coated and spray deposited films are almost identical and show a main peak at the same position. The peak position shifts after the template is removed to higher q-values, indicating that the structure shrinks in size. After the template removal the peak intensity is increased, attributed to a larger contrast between titania and the empty pores as compared to the organic template.

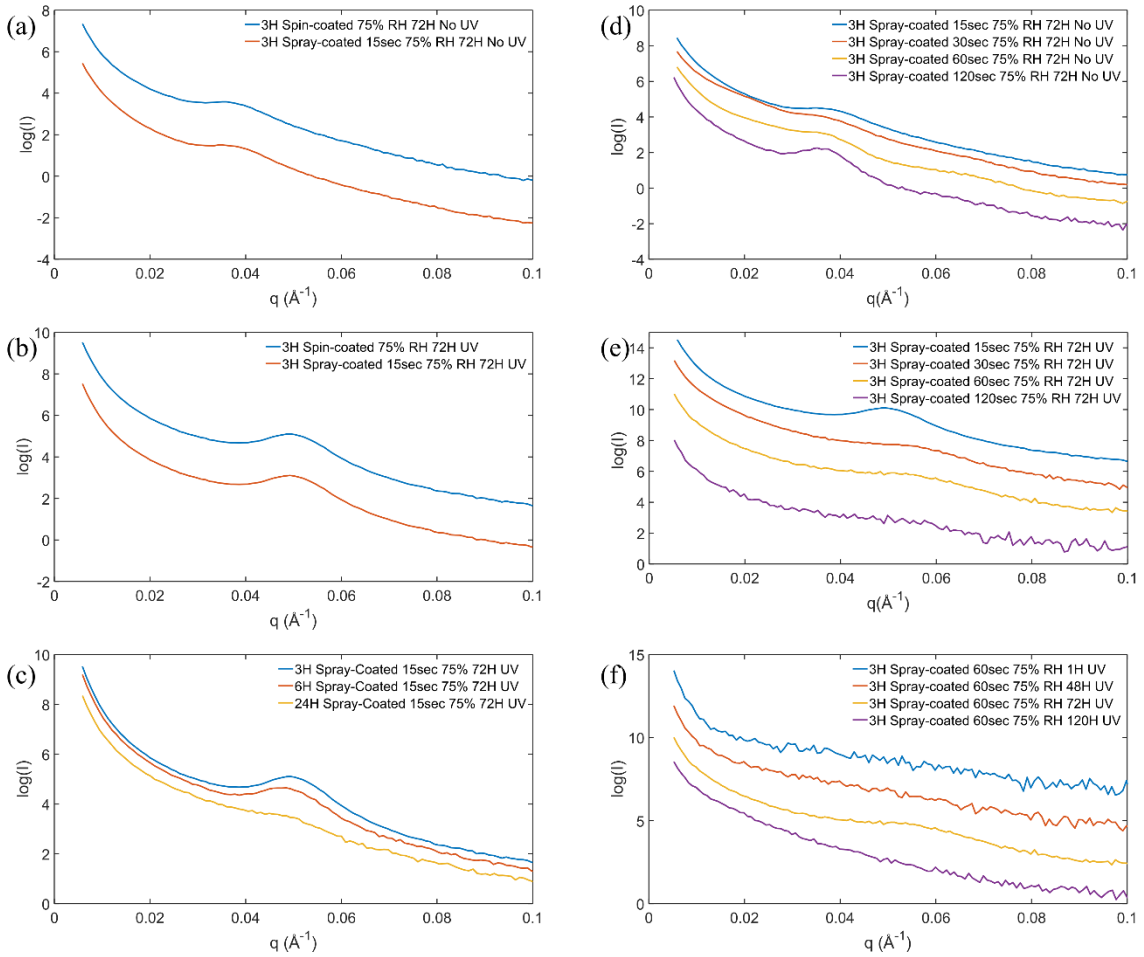

Figure 13. SAXS patterns of samples prepared with either spin-coating or 15 seconds of spray-coating from solution with 3 hour synthesis time, before template removal (a) and after template removal (b). SAXS patterns of 15 seconds spray-coated films prepared from solution with reaction times from 3-24 hour, after template removal (c). SAXS patterns of films with 15-120 seconds spray-coated films before (d) and after template removal (e). SAXS patterns of 60 seconds spray-coated films with aging time 1-120 hours at 75% RH (f). The patterns are shifted in intensity for clarity.

To more thoroughly evaluate the morphology and crystal structure of the spray coated mesostructured titanium dioxide, TEM was employed. Figure 14 shows micrographs of samples before template removal (a) and after template removal (b), showing the hexagonal order of the pores. The pore size is measured 6.5 nm before template removal and 5.5 nm after removal, corroborating the SAXS results. Figure 14f shows (HR)TEM image of the same sample where the crystallinity is clearly observed, and the d-spacing suggests the crystals are of the anatase polymorph. The SAXS patterns and the TEM characterization demonstrate that hexagonally ordered mesoporous titania films were successfully prepared by the low-temperature spray deposition method.

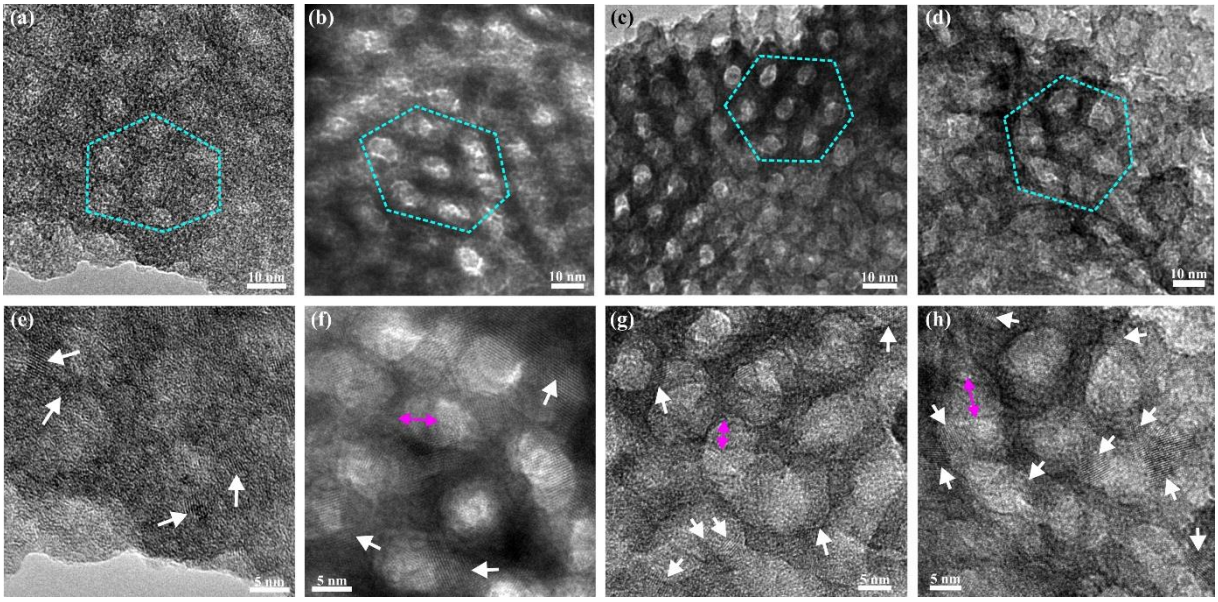

Figure 14. (BF)TEM images of mesostructured titania with synthesis times 3 hours without template removal treatment (a), and with synthesis times of 3 hours (b), 6 hours (c) and 24 hours (d) and subsequent template removal treatment. The hexagonal order of the pores has been outlined with cyan dotted lines. (e-h) are (HR)TEM images of samples (a-d), respectively in which the anatase crystalline areas are denoted by the white arrows. Magenta double arrows denote the shadowing of the pores due to the inclined viewing direction.

7.2 Effect of synthesis time on mesoorder and atomic order

The synthesis time at 40 °C, before the film deposition, was varied from 3-24 hours and the effect on the mesostructure was analyzed with SAXS measurements and TEM imaging. Figure 13c shows SAXS patterns of titania films prepared from solutions with synthesis times of 3 and 6 hours, suggesting that the samples have a similar degree of mesoorder, and with synthesis time of 24 hours which shows a less sharp diffraction peak with a lower intensity, suggesting that the material has a lower degree of mesoorder. Figure 14(a-d) shows TEM images of the hexagonally ordered pores of the titania films. The films with 3 hours (b) and 6 hours (c) synthesis time clearly show hexagonal order, but the order appears to be more disrupted after 24 hours synthesis time (d). The hexagonal order is also observed before the template removal (a) but it is not as easily observed as the pores are filled by the polymer making the contrast lower. All samples exhibited the anatase titania polymorph and the crystallites are better defined after the template removal. This is depicted in the HR-TEM images of Figure 14(e-h). With increasing synthesis time the crystallites appear to have grown in size, and after 24 hours synthesis time the crystals have partly grown out of the walls and into the pores and distort the structure as can be seen from the distorted shape of the pores. This crystal growth can likely be

attributed to unreacted titania precursor species or within the hydrophilic domains of the liquid crystalline template.

7.3 Effect of aging time on mesoorder and atomic order

The effect of varying aging time at 75% relative humidity from 1 hour to 120 hours on the mesostructure and crystallinity of the films was studied. Figure 13f shows the SAXS patterns of the samples which suggests that ordered mesostructure is only achieved for the sample aged for 72 hours, but not for samples aged for 1 hour, 48 hours or 120 hours. TEM images shown in Figure 15 are in good agreement with the SAXS diffractograms, where a clear hexagonal order is observed in sample aged for 72 hours (c), but not in the other samples (a,b,d). The HR-TEM images show that films aged for 1 and 48 hours (e,f) appear to be mainly amorphous, but the pore walls also contain some small crystals of about 2 nm in size. The polymer template was not fully removed in those two samples, which we attribute to the limited photocatalytic activity of the amorphous and small crystals, which is essential to the UV template removal procedure.

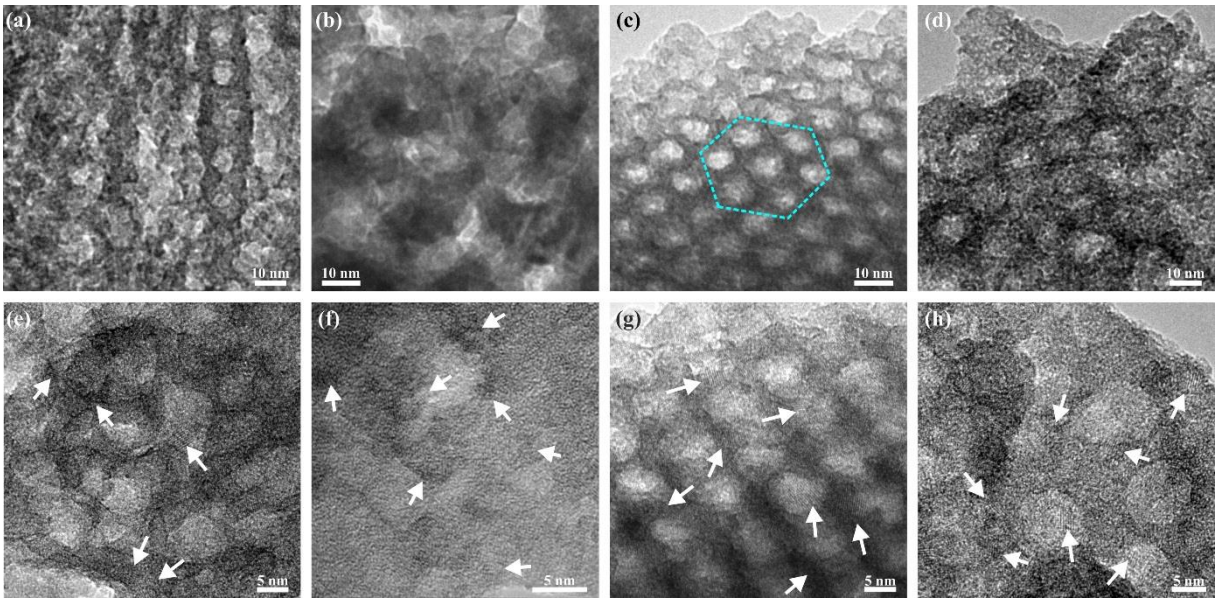

Figure 15. TEM images of mesoporous titania with 3 hour synthesis time, deposited with 60 seconds spray coating and aged at 75 % relative humidity for (a,e) 1 hour, (b,f) 48 hours, (c,g) 72 hours, and (d,h) 120 hours. Hexagonal pore order was achieved for the sample aged for 72 hours and is outlined with dotted cyan line (c). White arrows indicate anatase polymorph order.

It appears that after aging for 72 hours (g) the crystals have grown enough, to ca. 4 nm, to be able to photocatalytically remove the polymer template. The template is also removed for the sample aged for 120 hours, but the ordered pore structure appears to be completely lost. Figure

15(d,h) shows that the crystals have grown into the pores which appears to be the cause of the structural collapse. This shows unambiguously that the crystals gradually grow during the aging time at 75% relative humidity and there is enough driving force, even at room temperature, for the crystal growth to disrupt the structure of the mesoporous titania. These results show that the aging time is a critical parameter for the atomic order of the film, which in turn has a destructive effect on the pore order.

7.4 INFLUENCE OF FILM THICKNESS ON THE MESOORDER

The film thickness was controlled by varying the spray time onto the glass slide, from 15-120 seconds. Figure 13 shows the SAXS patterns of the films of different thicknesses before template removal (d) and after template removal (e). Before template removal, the SAXS patterns all show a main peak at 0.036 $Å^{-1}$, and the thicker films, with 30-120 seconds spray time, show a secondary peak at 0.064 $Å^{-1}$. The relative position of these peaks ($1:\sqrt{3}$) is in agreement with a H1 hexagonal structure before the template removal.[88] After the template is removed, only the main peak remains and it is shifted to higher q-values in all cases. The appearance of the secondary peak before the template removal suggests that the films have a higher degree of mesoorder prior to the template removal, and that the mesoorder decreases during the UV-treatment. The mesoorder appears to be better maintained in the thinner film after the template removal and the order becomes progressively more distorted with increasing film thickness, as observed from the less sharp peak features with increasing film thickness in Figure 13e. The thickness of the films, after the UV-treatment, was measured with a profilometer and the results are presented in Table 3.

Table 3. The film thickness of samples with 15 to 60 seconds spray time.

Spray time [sec]	Thickness [µm]
15	7 ± 1
30	13 ± 2
60	20 ± 2

8. LITHIUM ION BATTERIES

The increased availability and use of techniques that capture intermittent renewable energy sources demands efficient and reliable energy storage systems to be implemented in portable electronics, electric vehicles as well as stationary energy systems. Batteries store chemical energy and transform it to electrical energy when discharged, and the lithium ion battery (LIB) is a prominent energy storage solution for these applications due to its high energy and power density, as well as long cycle life and reasonable production cost. The high energy and power density of lithium ion batteries is based on the light weight of the metal and its large negative reduction potential. [89–91] Figure 16 shows a schematic of a lithium ion electrochemical cell with the flow of electrons and lithium ions (yellow circles) indicated by the arrows during lithiation (a) and delithiation (b).

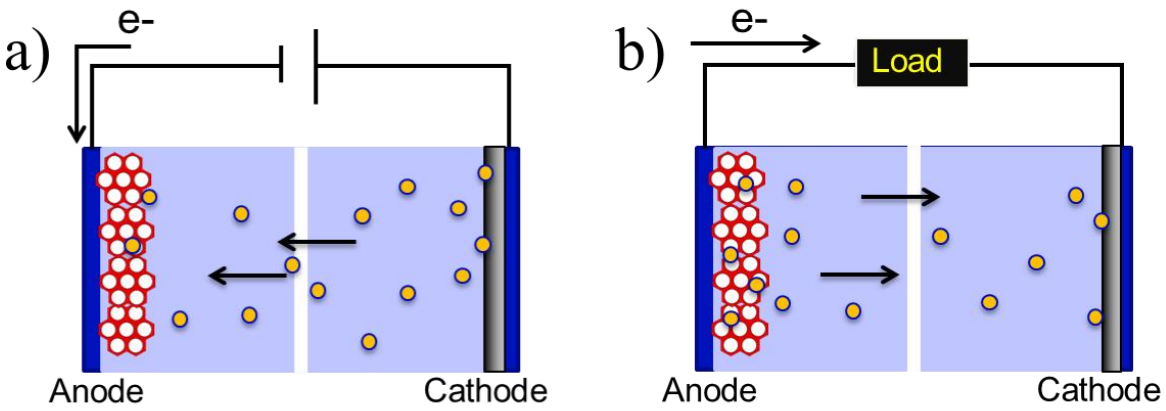

Figure 16. The main components of a lithium ion electrochemical cell. The flow of the lithium ions (yellow circles) and the electrons are indicated by the arrows in a) lithiation and b) delithiation.

The key components of the electrochemical cell are the anode, cathode, electrolyte and the separator. The anode and cathode are able to accommodate and release lithium ions. The

electrolyte is a conductor for the lithium ions between the cathode and anode during electrochemical reactions. The electrons are conducted through an external circuit. The separator prevents direct contact between the anode and the cathode, which would result in short circuit of the cell. The cathode, anode and electrolyte are the most important components that determine the performance of LIB and extensive research efforts have been dedicated to develop materials to improve the performance of these components with the aim to increase the capacity, the rate capabilities, the cycle life and safety.[92,93]

Graphite is the most commonly used anode material in lithium ion batteries. Li is intercalated between the graphene planes and up to 1 Li atom per 6 C atoms can be stored. The success of carbon as an anode material is attributed to its low cost, high electrical conductivity and lithium ion diffusivity, adequate energy density, power density and cycle life.[94,95] A number of other anode materials have been studied and a few of them are listed in table 4.

Table 4. Properties of a few commonly studied anode materials.

Material	Discharge capacity [mAh/g]	Potential (vs. Li/Li^+) [V]	Volume change [%]	References
Graphite	372	0.1	10	[95]
Si	4200	0.4	270	[95,96]
Sn	790	0.6	255	[95,97]
$Li_4Ti_5O_{12}$ (LTO)	175	1.6	0.2	[95]
Titania anatase	196*	1.0	3	[98,99]

*tested at 0.2 C

Silicon (Si) and tin (Sn) based anodes have caught the interest of researchers due to their exceptionally high theoretical capacity, but during lithiation these materials go through large volume expansion, increasing their original volume by several times.[100–103] These large volume changes as the material is lithiated and delithiated, cause stress fractures and leads to cracking of the solid electrolyte interface (SEI) layer and results in rapid capacity fading.

Despite offering a lower capacity, lithium titanium oxide or LTO ($Li_4Ti_5O_{12}$), has been studied and used commercially in electric vehicles, electric bikes and in medical devices. Their success is mainly attributed to their high rate capabilities, thermal stability and long cycle life which originates from a negligible volume change in the material during lithiation and delithiation and the high lithiation potential. The operational potential window of the cell is therefore high, minimizing the formation of SEI, avoiding lithium dendrite formation even at high charge/discharge rates.[95]

Recently, titania has been explored as anode material in lithium ion batteries. At the high operational potential the electrolyte decomposition and lithium dendrite formation is avoided and due to a very small volume expansion when lithiated, titania delivers a stable performance over many cycles. However, the electrical and lithium ion conductivity of bulk titania is low which causes a rather poor rate capability of the material. Nanostructured titania with high surface areas and short ion diffusion paths have been designed to circumvent this challenge, offering high surface areas and short ion diffusion paths.[11,104] In addition, the extent of lithiation and the lithiation diffusion is affected by the titania polymorph type. For both anatase, rutile and TiO_2-(B) polymorphs, nanostructures have shown higher capacity and better performance than the respective bulk phase.[105–110] For all polymorphs, the lithium insertion into titania is described by eq.

$$xLi^+ + TiO_2 + xe^- \leftrightarrow Li_xTiO_2 \qquad (17)$$

where $0 \leq x \leq 1$. The theoretical maximum capacity of titania anatase is calculated from x=1, to be 335 mAh/g.[84] The relatively open anatase structure is considered a promising candidate as a lithium host. The structure of anatase, which can be viewed as stacked zigzag chains consisting of distorted edge-sharing TiO_6 octahedrals, contains pathways for the lithium ion to diffuse through and the ions can occupy the interstices of the TiO_6 octahedra. A phase transition of the anatase phase occurs at $x \approx 0.05$, but the displacement of the atoms is relatively small and the unit cell volume increase is only about 4%.[98,99] Conversely, the lithiation of the rutile polymorph is more challenging. This is due to the slow and anisotropic diffusion of lithium ions into the structure, which originates from the octahedral sharing which provides a one dimensional pathway (c-axis) but significantly slows down the diffusion in the a/b planes. In general much lower capacity is obtained for the rutile polymorph.[107,108] Lithium insertion has been studied in a few other titania structures, including the TiO_2-(B) polymorph and amorphous titania. In the case of amorphous titania, it tends to exhibit high capacity in the first cycle, about double the theoretical maximum capacity of titania but the capacity decreases rapidly in the following cycles.[111,112] The structure of amorphous titania has been characterized as having an atomically ordered core and a large number of defects near the surface and that the average coordination number of the titanium atom is lower close to the surface.[113,114] Additionally, amorphous titania displays a linear correlation between voltage and capacity from about 2 V,

which is very different from the distinct potential plateaus corresponding to redox reactions observed in crystalline titania.[115]

8.1 LITHIUM INSERTION IN MESOPOROUS TITANIA

In **Paper 3**, the lithiation of spray deposited ordered mesoporous titania was studied and compared to crystalline anatase nanoparticles for reference. The material is composed of anatase nanocrystallites, about 3-4 nm in size, and amorphous titania. The mesoporous structure of the material provides short lithium ion diffusion paths and easier access to the lithium intercalation sites. The synthesis and characterization is detailed in Chapter 7 and in **Paper 2.** Chronopotentiometry and cyclic voltammetry measurements were performed to characterize the lithiation and delithiation and to investigate the observed capacity fading. Further, the structural characterization was conducted prior to and after electrochemical cycling to examine the structure and the structural changes the material experiences during cycling. In **Paper 3**, the studied anode consists of titania, mesoporous or anatase nanocrystalline, mixed with Carbon Black, Super-P™ and Kynar® PVDF binder, the electrolyte is a commercial LP30 (1M lithium hexafluorophosphate in EC/DMC 50/50 (v/v))) and glass microfiber was used as a separator. The titania was tested in a half cell configuration, where a lithium disc was used as the counter electrode. In this configuration, the lithium disc is defined as the anode and the titania electrode is defined as the cathode. This reverses the definition of the charge/discharge in our experimental configuration compared to the definitions when using titania as anode material. To avoid misinterpretation, these processes are referred to as lithiation and delithiation when possible. Further experimental details are found in the manuscript and in chapter 5.3.

Figure 17 shows the charge/discharge curve of mesoporous titania (a) and nanocrystalline anatase (c) when cycled between 2.9 V and 0.7 V and 2.9 V and 1.0 V, respectively. Voltage plateaus are observed at 1.95 V, lithiation, and 1.75 V, delithiation, for anatase. Conversely, the mesoporous titania exhibits a quasi linear dependence of the stored charge with the potential during the lithiation/delithiation and a very high capacity of ~680 mAh g^{-1} is obtained in the first lithiation cycle but the capacity decreased rapidly in the following cycles. These features are further highlighted in the CV curves, where well-defined redox peaks are observed for the anatase nanopowder (Figure 17d) but no distinct peaks for the mesoporous titania (Figure 17b). This type of charge/discharge behavior is defined as pseudocapacitive behavior of intercalation type in a recent publication.[116]

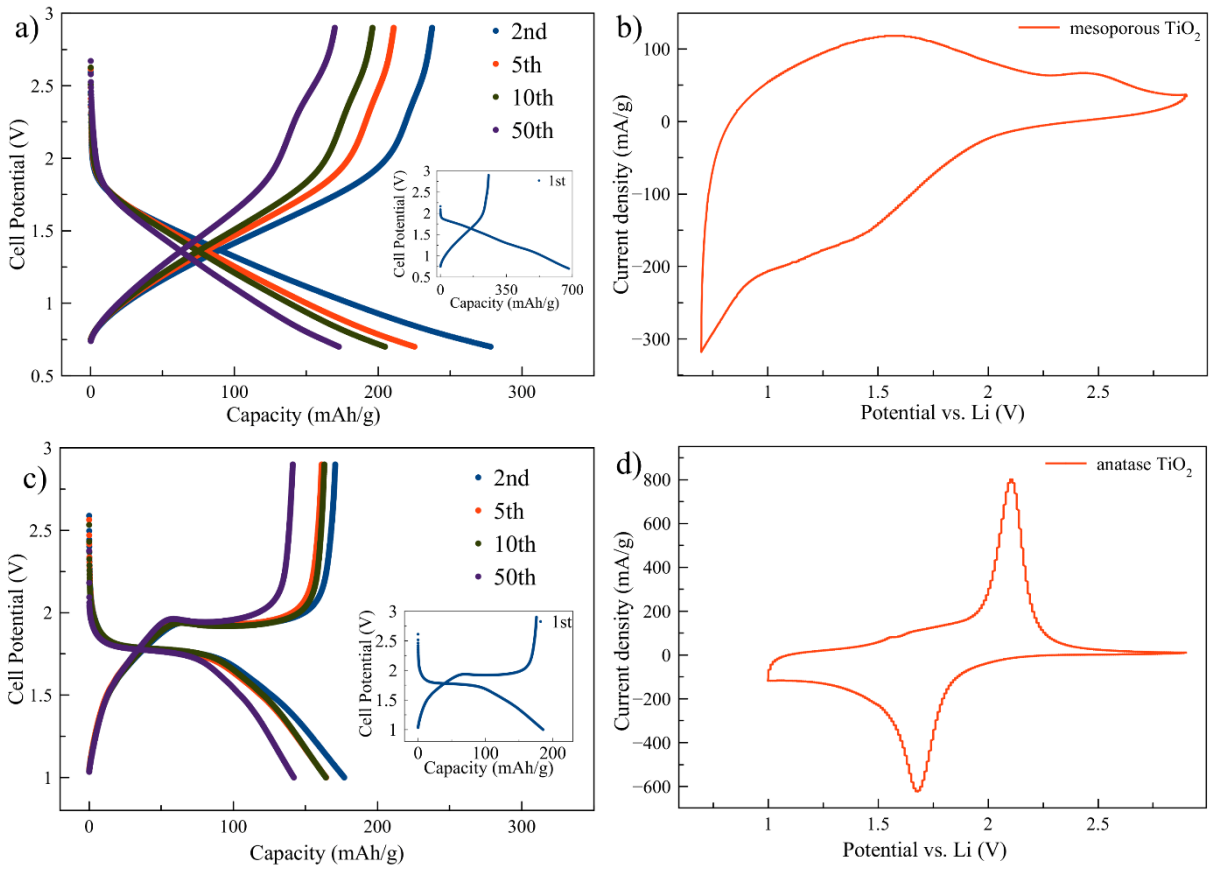

Figure 17. Charge/discharge curves of mesoporous titania electrodes between 2.9 V and 0.7 V (a) and anatase titania electrodes between 2.9 V and 1 V (c) both cycled at 0.5 C. Cyclic voltammetry curves (10th cycle) scanned between 2.9 V and 0.7 V for mesoporous titania (b) and scanned between 2.9 V and 1 V for anatase (d) at scan rate 0.3 mV/s.

The mesoporous titania shows good rate capability, delivering ~83 mAh g^{-1} at 10 C, and the material recovers its higher capacity when cycled at lower rates again, suggesting that the fast cycling does not damage the structure of the material. The capacity retention between cycle 20 and 200 was found to be ~80%.

To further investigate the lithium intercalation and the irreversible capacity of the mesoporous titania, CV measurements with cutoff voltages between 2.9 V and 1.7, 1.3, 1.0 and 0.7 V were performed and the first and fiftieth cycles are shown in Figure 18. The measurements reveal that the irreversible capacity occurs even when the mesoporous titania is cycled between 2.9 V and 1.7 V. To investigate the origin of the peaks and the associated structural changes, further characterization of the samples before and after cycling was performed with TEM and XAS.

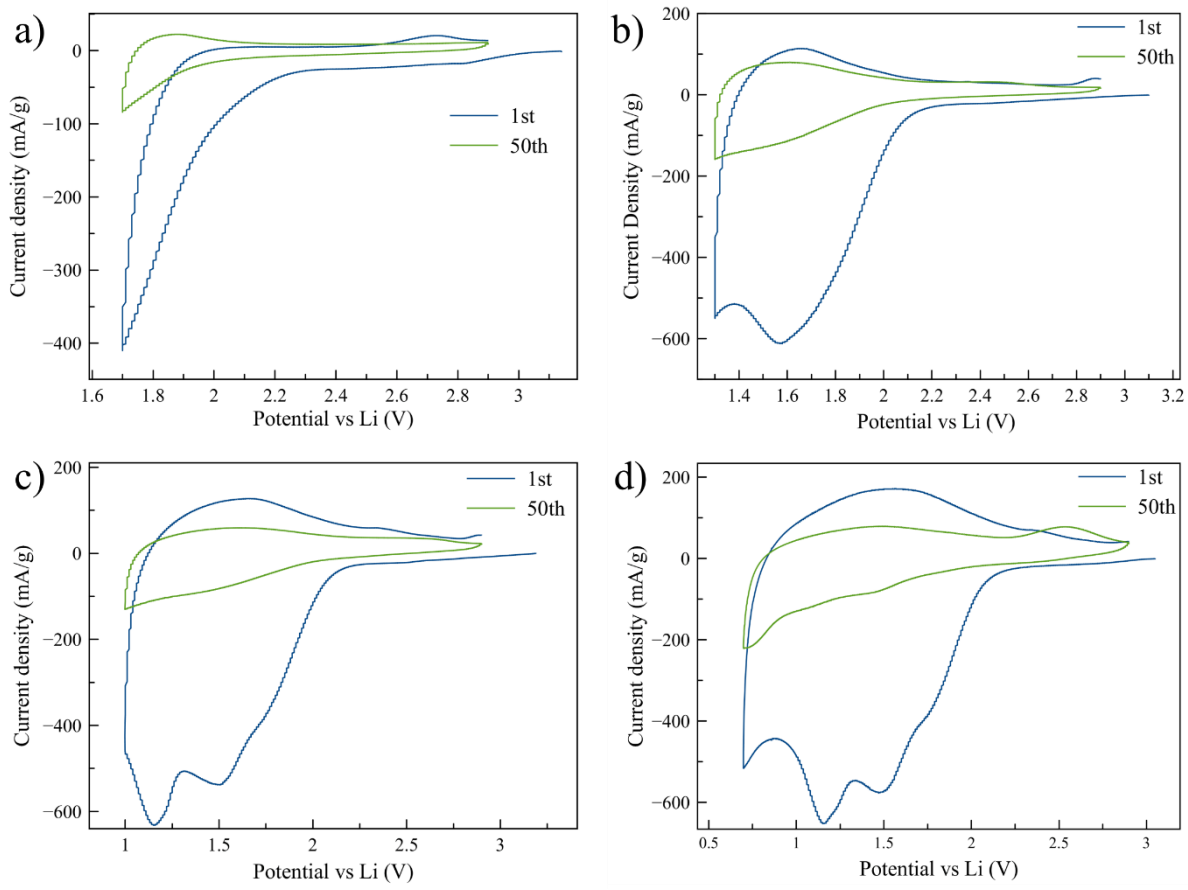

Figure 18. Cyclic voltammetry scans performed with a three-electrode setup at 0.3 mV/sec between 2.9 V and 1.7 V (a), 2.9 and 1.3 V (b), 2.9 and 1.0 V (c), and 2.9 and 0.7 V (d). The first and fiftieth cycle of each CV are shown in the graphs.

Figure 19 shows the X-ray absorption spectra of the titanium K-edge before cycling and after cycling between the voltage limits shown in the CV scans. From the measurements of the samples before cycling, the average coordination of the titanium atom was determined to be between 5 and 6 in the mesoporous titania sample and 6 in the anatase sample. After cycling for 50 cycles, the cycling was interrupted at 2.9 V which corresponds to the total delithiation (of the reversibly stored Li). In addition, a sample was prepared by interrupting the cycle at 0.7 V after cycles, corresponding to the most lithiated state studied here. The samples interrupted in the delithiated state, no shift in the absorption edge was observed, suggesting that the oxidation state of titanium remains the same, +4. For the sample interrupted in the lithiated state (intercalated state) the edge position shifted to lower energy, and the average oxidation state was estimated to +3.77 (Figure 19b). This suggests that the reversibly bound lithium affects the Ti oxidation state, but the irreversibly bound lithium does not.

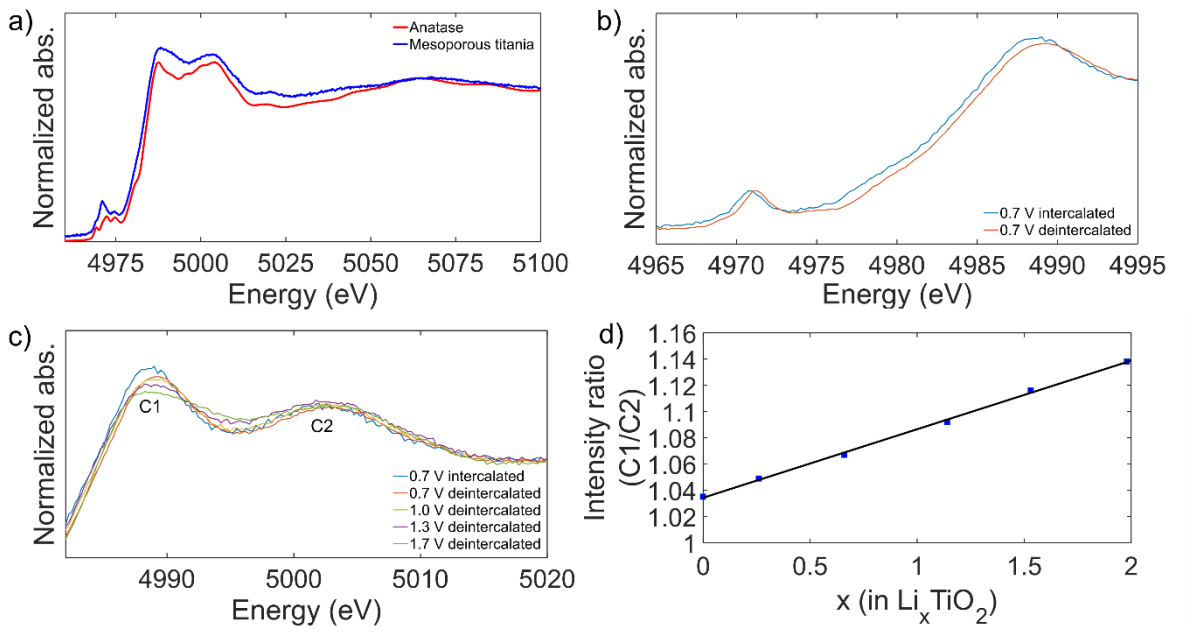

Figure 19. XAS spectra of the anatase and the pristine mesoporous titania samples (a). Comparison of the samples cycled between 2.9 V and 0.7 V, interrupted in the intercalated and the deintercalated state, showing a shift in the edge position (b). The post-edge region of the XAS spectra of pristine and cycled mesoporous titania is highlighted (c) and the effect of the lithium concentration on the peak intensity ratio C1/C2 (d). The point at x=0 is for the pristine sample.

In the post-edge region, highlighted in Figure 19c, it is observed that cycling the samples leads to increased peak intensity ratio, C1/C2, and the intensity increases with lower cutoff potential. Moreover, the sample cycled to 0.7 V in the lithiated state has a higher peak ratio than the sample in the delithiated state. The electrochemical measurements showed a large irreversibility during cycling, implying that lithium is irreversibly inserted in the electrode and the amount of lithium in the electrodes in the deintercalated state is calculated as the difference in the specific capacity of the first and the fiftieth cycle. For the sample in the intercalated state, containing both irreversibly and reversibly bound lithium, the lithium concentration is calculated as the specific capacity of the first reduction curve. Figure 19d demonstrates the linear relationship between the lithium concentration and the intensity ratio of the peaks C1/C2. The linear relationship suggests that the local environment of the titanium atom is affected in a similar way by the irreversibly and reversibly bound lithium and the distance between the titanium atom and the intercalated lithium atom is very similar in both cases. Moreover, this implies that the formation of lithium containing species outside the near environment of titania, such as lithium oxide, is improbable. Due to the linear relationship, the XAS measurements can be used to quantify the amount of lithium inserted into the titania structure. Conversely, a deviation from linearity can be used to quantify the relative amount of lithium in the close proximity as well as lithium located further from the titanium atom.

TEM imaging and elemental mapping was used to further characterize the cycled samples in the delithiated state. Figure 20 shows BF TEM images of the sample cycled to 1.7 V. Carbon particles of average size ~55 nm and anatase nanocrystallites, ~3 nm, were observed. The presence of lithium titanate (Li_1TiO_2) was confirmed, in a sample cycled between 2.9 V and 1.0 V and in a sample cycled between 2.9 and 1.7 V. This suggests that the reduction peak observed at 1.7 V in the CV is associated with the formation of lithium titanate which appears to be, at least partly, responsible for the irreversible capacity. It appears that the lithium titanate crystals are formed by local crystallization phenomena as the phase is found in the sample cycled to 1.7 V, which has an average concentration of Li below x = 1 in Li_xTiO_2. The presence of Li_xTiO_2 further supports the XAS results, which suggested that the irreversibly bound lithium is indeed in close proximity to the titanium atom.

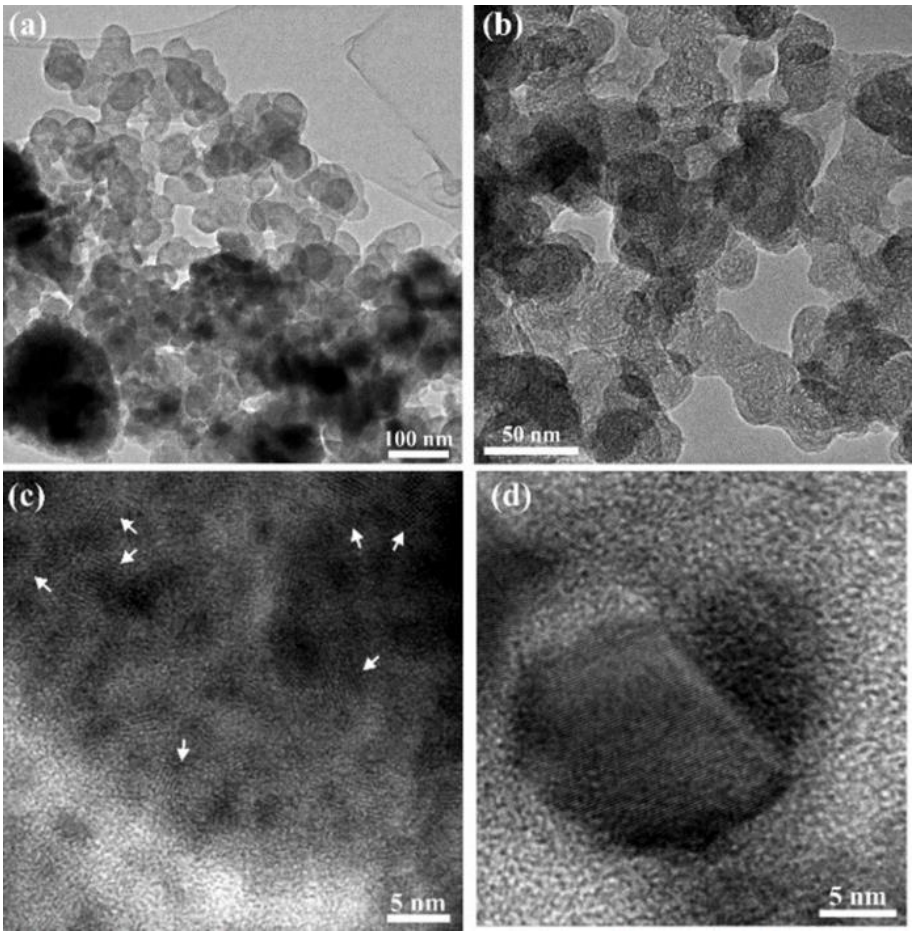

Figure 20. Bright field TEM images of the electrode cycled to 1.7 V showing the overall morphology of the sample (a, b) and HR-TEM images showing the nanocrystalline anatase (c) and $LiTiO_2$ (d).

Energy filtered (EF) TEM experiments were performed to further examine the electrode, the amorphous phases and the distribution of the irreversibly bound lithium. Elemental maps of C, Li, Ti and O and the composite maps are shown in Figure 21.

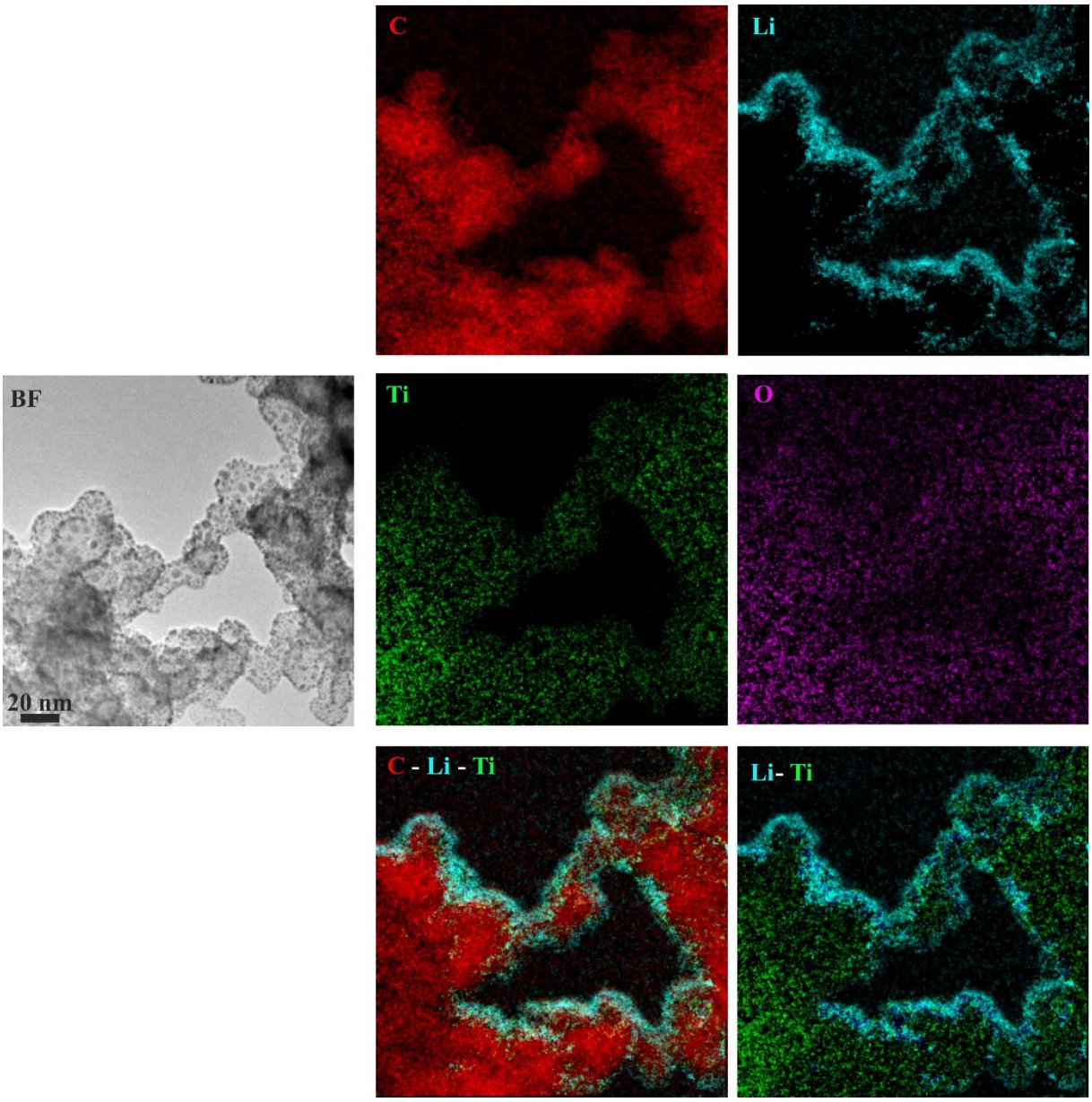

Figure 21. Unfiltered (BF), energy filtered images, and composite elemental maps of the mesoporous titania cycled to 1.0 V. From the composite elemental maps it can be seen that Li appears to be located mainly at the surface while Ti, C and O are distributed over the whole area. The scale is the same for all images.

The individual and composite elemental maps show that Li appears to be located mainly at the surface while Ti, C and O are distributed over the whole area. Considering the nature of the amorphous titania phase, which contains a large number of defects near the surface, and the lithium elemental map, it appears that the irreversible phases are mainly located at the surfaces.

Moreover, the composite maps show that lithium is located in close proximity of titanium and oxygen, which is in line with our hypothesis that irreversible Li_xTiO_2 species are formed during the cycling.

9. SYNTHESIS OF MESOPOROUS SILICA FILMS

In **Paper 4** we investigated the effects various synthesis parameters, such as the hydrolysis time of the silica precursor and mixing time of the hydrolyzed precursor and the block copolymer, have on the mesoorder of silica films prepared by spray deposition at room temperature. The mesoporous silica films, similar to mesoporous titania films, were formed via EISA by spray coating the solution of the surfactant and the silica precursor on a surface. The advantages and challenges of the deposition method and the processing parameters that were used are described in section 5.1. Figure 22 shows the phase diagram of the water, ethanol and block copolymer system used.

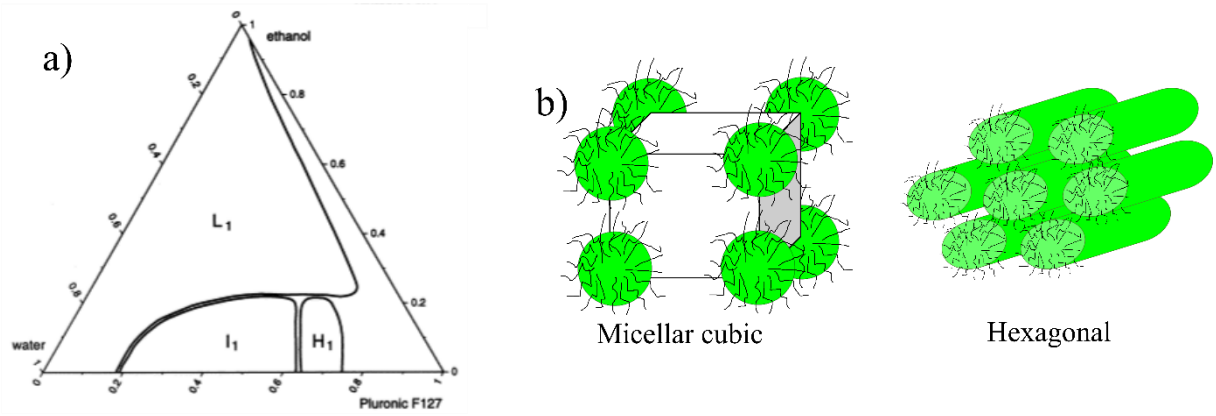

Figure 22. (a) Ternary phase diagram of the water, ethanol and Pluronic™ F127 system. L_1 denotes the isotropic liquid region, I_1 denotes the cubic region and H_1 denotes the hexagonal region. The phase diagram is adopted from reference.[58] (b) Schematic illustration of the cubic and hexagonal mesostructures.

Assuming full hydrolysis of the silica precursor, the synthesis solution is located in the isotropic liquid region, L_1, before deposition. In the study, two series of samples were prepared. In series A, the silica precursor, TEOS, was hydrolyzed in an acidic aqueous solution and the solution was stirred for 5 hours, after which the block copolymer Pluronic™ was added and spray deposited samples were prepared at selected time intervals following the addition of the

polymer. In series B, the hydrolysis time of TEOS was varied as 2, 3, 4 and 5 hours whereas the mixing time with the copolymer was fixed to 3 hours. SAXS measurements were carried out to characterize the mesostructure of the spray deposited films and to evaluate the effect of the hydrolysis time of the silica precursor and the mixing time with the block copolymer on the mesoorder. Figure 23 shows the SAXS patterns from series A (a) and series B (b). The labels on the patterns in (a) refer to time from addition of the polymer to the spray deposition of the sample. The labels in (b) refer to the time from start of the hydrolysis to the addition of the copolymer.

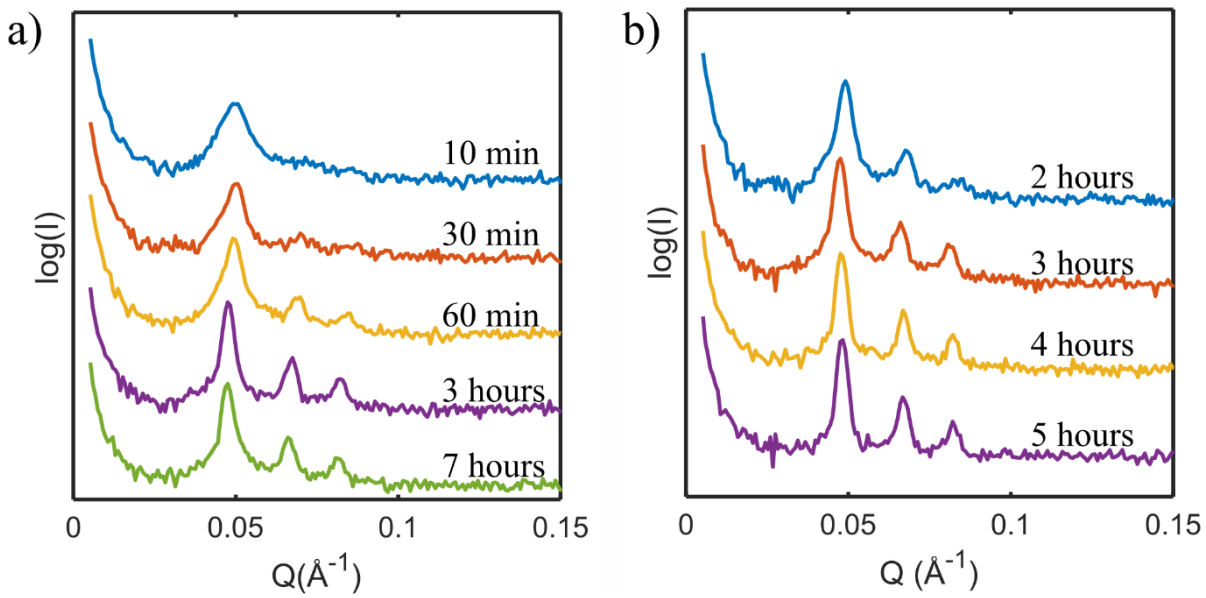

Figure 23. SAXS patterns of spray deposited silica films. (a) Silica precursor was hydrolyzed for 5 hours before addition of block copolymer and mixed for 10 minutes, 30 minutes, 60 minutes, 3 hours or 7 hours, respectively, before spray deposition. (b) Silica precursor hydrolyzed for 2, 3, 4 or 5 hours, respectively, and mixed with the block copolymer for 3 hours before spray deposition.

In series A, where the hydrolysis time was fixed to 5 hours, the first film was prepared by spray depositing the synthesis solution 10 minutes after adding the polymer to the mixture, which was the time it took the polymer to fully dissolve. In Figure 23a, a single broad peak is observed, denoted 10 min, showing that the film has some degree of mesoorder when deposited immediately after the polymer was dissolved. With increasing mixing time, two additional peaks emerge and the diffraction peaks become sharper after 3 and 7 hours mixing times. In series B, where the mixing time was fixed to 3 hours, 3 peaks are observed for the sample with 2 hours hydrolysis time, shown in Figure 23b. All peaks become sharper and the second and third peaks become more intense for the samples with longer hydrolysis time, suggesting a higher degree of mesoorder. This demonstrates that higher degree of condensation of the silica

precursor prior to adding the copolymer results in higher degree of mesoorder. The peak position ratio is 1:√2:√3, in both series, which is associated with cubic structures.[117,118] These results are consistent with the phase diagram, suggesting a shift in the phase diagram from the isotropic region, L_1, to the cubic region due to the evaporation of the solvents during the spray deposition. Spray depositing the solution with 5 hours hydrolysis time and 3 hours mixing time with the block copolymer resulted in highly ordered mesostructured films.

The last step in the synthesis of the spray deposited mesoporous silica is removing the polymer template, which was carried using heat treatment. To evaluate the effect of the heat treatment on the mesoorder, films were prepared from the synthesis mixture with 5 hour hydrolysis time of the silica precursor and 7 hour mixing time with the polymer. This synthesis solution was chosen due to its high degree of mesoorder prior to the calcination. After spray deposition on glass slides, the sample was heated in an oven at 80 °C for 2 hours and subsequently calcined at 500 °C, temperature increase appr. 1 °C/min and kept at 500 °C for 6 hours. In addition, a film was prepared and aged at 75 % relative humidity for 16 hours prior to the heat treatment. The films were scraped of the glass slides and transferred to a quartz capillary for SAXS measurements. Figure 24 depicts the SAXS patterns of the calcined sample prior to calcination, after calcination and the sample that was stored at high RH prior to calcination.

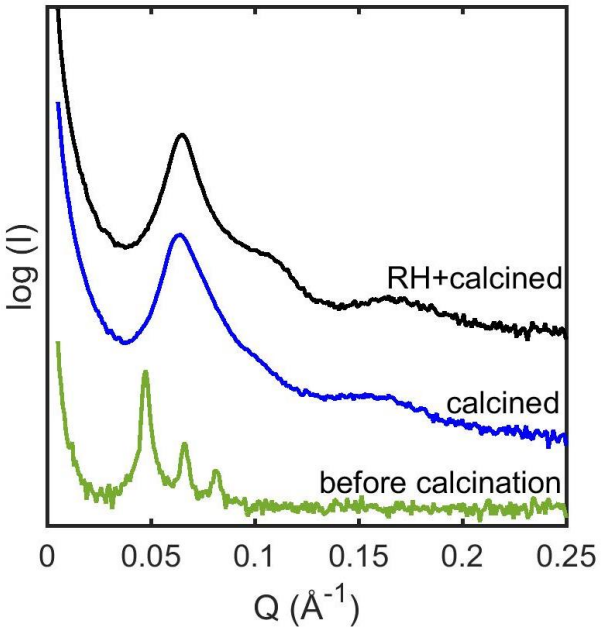

Figure 24. SAXS patterns of the films prepared from solution with 5 hour hydrolysis time and 7 hour mixing time before calcination (green trace), after calcination (blue trace) and a sample that had been kept at 75% RH for 16 hours and subsequently calcined (black trace).

The patterns of both calcined samples show much broader features than the pattern that was obtained before calcination, which implies that the calcined samples have a lower degree of mesoorder. Additionally, the peak position is shifted to larger *q* values compared to the sample that was not calcined, which is expected as calcination typically leads to contraction of the mesostructure. The additional step of aging the films at high RH prior to the heat treatment results in a narrower first peak and a better defined shoulder peak suggesting that aging the films increases the mesoorder of the calcined films. The SAXS peak position pattern of the calcined films is 1:√3:√7 which is similar to the peak pattern associated with a hexagonal structure (1:√3:2:√7). The results suggest that the calcination causes the mesoorder of the film to shift from a cubic structure to a hexagonal structure, which is further supported by the phase diagram which contains a hexagonal region at polymer concentrations between 65 and 75 wt.%, at slightly higher concentration than the cubic region. The solvents, ethanol and water, are evaporated during the heat treatment causing the composition of the film to shift from the cubic region to the hexagonal region and changing the mesoorder of the film in addition to decreasing the degree of mesoorder. The morphology of the films was examined with TEM and Figure 25 shows micrographs of the mesoporous silica film prepared from the film aged at high RH and calcined. In (a), a low magnification image shows a large continuous particle, several hundred nm or several μm in size. The pore size is 5.6 ± 1 nm. The mesoorder of the film is not clearly observed in the images.

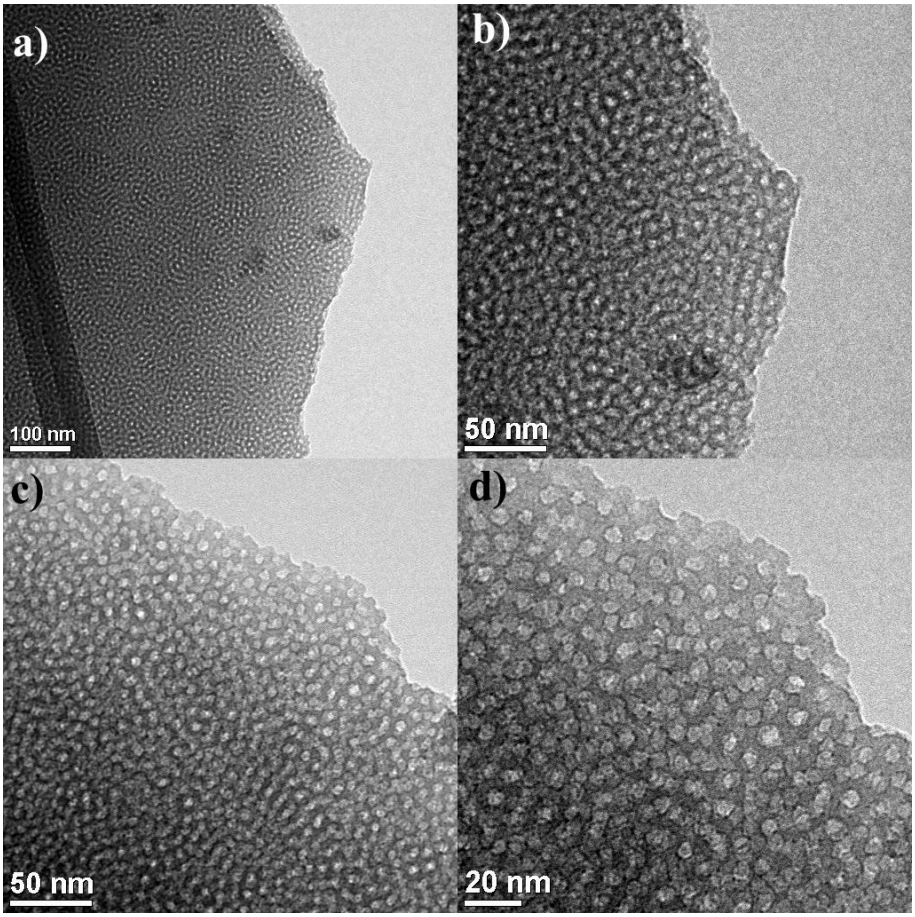

Figure 25. Bright field TEM images of calcined mesoporous silica film prepared from solution with 5 hour hydrolysis of the silica precursor time, 7 hour mixing time with the polymer and aged at high RH prior to calcination at low magnification (a) and higher magnification (b-d)

The structure parameters of the mesoordered silica films, prior to and after calcination, were determined from the SAXS diffractograms and the TEM images and are listed in table 5.

Table 5. The structure type and d-spacing of the films prior to and after calcination estimated from SAXS measurements. The non-calcined sample refers to the film prepared from solution with 5 hour hydrolysis time and 7 hour mixing time with the polymer.

Sample	Structure type	d-spacing [Å]
Non-calcined	Cubic (primitive)	133
RH+calcination	Hexagonal	96 (100*)

*Estimated from TEM micrographs.

The *d*-spacing of the calcined film, which corresponds to the distance between two planes of cylinders in a hexagonal structure is given by the formula,

$$d = \frac{2\pi}{q} \qquad (18)$$

where q is the peak position of the first and most intense peak. The peak pattern for the non-calcined films is associated with two types of cubic structures, primitive cubic and body centered cubic. The lattice spacing of each cubic structure was determined by plotting the reciprocal spacing, d_{hkl}, of the reflection peaks versus the sum of the Miller indices $(h^2+k^2+l^2)^{1/2}$, shown in Figure 26. The indexing of the peaks is different between the primitive and the body centered cubic, resulting in different lattice parameter. By comparing the calculated d-spacing of the two structures to literature values we suggest that the structure is a primitive cubic.

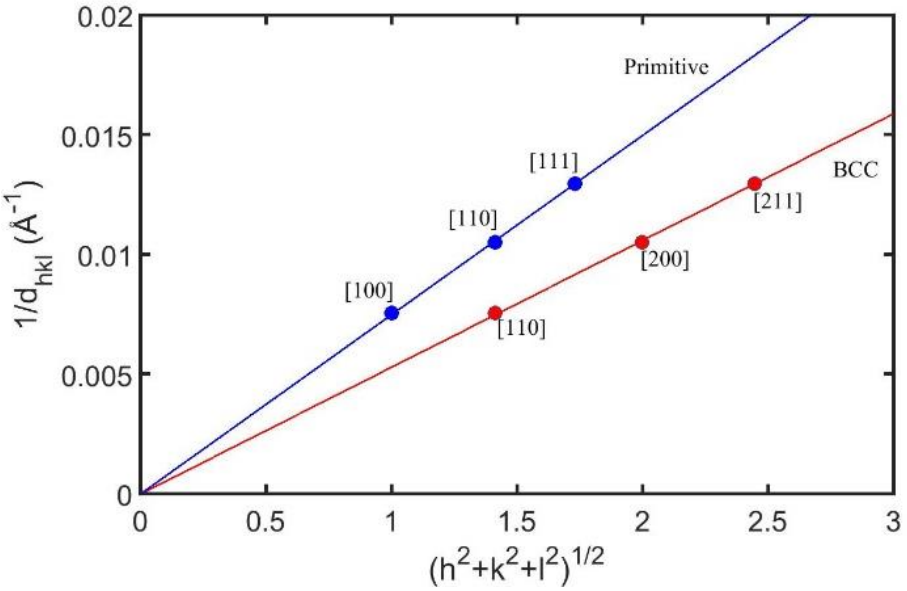

Figure 26. The reciprocal, d, of the reflections plotted versus the sum of the Miller indices of the primitive and body centered cubic unit cells.

10. CONCLUDING REMARKS

The focus of this work was on developing and studying syntheses of nanostructured titania and silica, and to evaluate mesoporous titania as an anode material in lithium ion batteries. The effect of selected relevant synthesis parameters on the structure of the powders and films were systematically studied and a low-temperature spray deposition method was developed to prepare mesoordered films of titania and silica.

The spray deposition method has the advantages that it is scalable to form evenly distributed films over large surfaces, the film thickness is tunable, surfaces of various shapes can be coated and heat sensitive substrates can be used. We demonstrated that by developing spray deposition protocols and synthesis solution compositions, ordered mesoporous silica and titania films can be prepared. In addition to establishing the viability of the method to prepare mesoporous titania, the effect of synthesis time prior to deposition, aging time at high relative humidity after deposition and film thickness on the crystallinity and mesoorder were studied. The results show that the synthesis time and aging time have to be carefully controlled to achieve the desired crystallinity in the films, and that the crystallinity, in turn, affects the mesoorder of the film. For the preparation of mesoporous silica films, the effect of the condition of the silica precursor, *i.e.* the degree of condensation of the silica precursor, the mixing time with the copolymer and the calcination of the film on the mesoorder were investigated. It was found that higher degree of condensation of the silica precursor prior to mixing with the polymer resulted in higher degree of mesoorder within the range studied, in agreement with previous work performed in the group. The mesoorder was also found to increase with increasing mixing time between the silica precursor and the copolymer. The degree of mesoorder decreased by calcining the sample, to remove the copolymer, but it was found that aging the film at high relative humidity prior to calcination decreased the loss of mesoorder.

Mesoporous titania was investigated as an anode material for Li-ion batteries. The material showed exceptionally high initial electrochemical capacity and good performance at high rates. A rapid decrease in capacity following the first cycle was observed and through electrochemical testing and structural characterization we suggest that formation of irreversible bound lithium in close proximity of the titanium atom is largely responsible for the irreversibility.

Titania nanoparticles were synthesized under acidic and low-temperature conditions and the effect of precursor concentration on the polymorph selectivity was evaluated. An unusual polymorph selectivity was observed. The rutile polymorph was initially formed, when the titania precursor concentration was high, but the brookite and anatase polymorphs, which are usually associated with kinetically favored formation, formed later, when the precursor concentration was lower. It was demonstrated that a solid-solid transformation or a dissolution-crystallization transformation process is improbable and that anatase and brookite formation instead occurs from the unreacted precursor in the solution.

11. ACKNOWLEDGEMENTS

This work has been carried out with gratefully acknowledged funding from the Swedish Energy Agency (Energimyndigheten) through project 38340-1.

I thank Landsvirkjun Energy Research Fund for financial support.

My supervisor Anders Palmqvist for giving me the opportunity to pursue my doctoral studies at Chalmers, for your support and trust which has motivated me in my work.

My examiner Martin Andersson for your engagement in the work and for encouraging words.

The directors of studies Hanna Härelind and Lars Nordstierna for support during my studies.

Giulio for the collaboration and all the good times, you really made the work more enjoyable!

Sanna Sommer for welcoming me in Aarhus and for the XRD and Rietveld analysis discussions.

Antiope Lotsari, Björn Elgh, Carmen Cavallo and Walter Rosas for your efforts in this work, I have learnt a lot from all of you.

Frida, Carina and Ann for the help with all administrative work and Romain and Mats for all the help in the lab.

All the people at Chalmers and Applied Chemistry for the good times and many fikas! Sam, Anand, David, Milene, Ting, Yifei, Caroline, Saba, Sanna, Andrey, Joakim, Florian, Ralph and many, many more. I am thankful for the great atmosphere you have created.

My friends outside the chemistry world for being awesome.

My family for encouraging me to pursue whatever I want to do and showing interest in what I work with, but mostly I am grateful because you made me who I am today.

Eva, thank you for your love and understanding. You mean the world to me.

12. REFERENCES

(1) Agency for Natural Resources and Energy. Energy Statistics. **2017**.

(2) IPCC. *Climate Change 2014: Synthesis Report. Contribution of Working Groups I, II and III to the Fifth Assessment Report of the Intergovernmental Panel on Climate Change*; 2014.

(3) Heeger, A. J. 25th Anniversary Article: Bulk Heterojunction Solar Cells: Understanding the Mechanism of Operation. *Adv. Mater.* **2014**, *26* (1), 10–28.

(4) Yan, J.; Saunders, B. R. Third-Generation Solar Cells: A Review and Comparison of Polymer:Fullerene, Hybrid Polymer and Perovskite Solar Cells. *RSC Adv.* **2014**, *4* (82), 43286–43314.

(5) Grätzel, M. Dye-Sensitized Solar Cells. *J. Photochem. Photobiol. C Photochem. Rev.* **2003**, *4* (2), 145–153.

(6) EG&G Technical Services Inc. *Fuel Cell Handbook,* Seventh Ed.; 2004.

(7) Armand, M.; Tarascon, J. M. Building Better Batteries. *Nature* **2008**, *451* (7179), 652–657.

(8) Greenwood, N. N.; Earnshaw, A. *Chemistry of the Elements*, Second Edi.; 1997.

(9) Fujishima, A.; Honda, K. Electrochemical Photolysis of Water at a Semiconductor Electrode. *Nature* **1972**, *238* (5358), 37–38.

(10) O'Regan, B.; Grätzel, M. A Low-Cost, High-Efficiency Solar Cell Based on Dye-Sensitized Colloidal TiO2 Films. *Nature* **1991**, *353* (6346), 737–740.

(11) Su, X.; Wu, Q.; Zhan, X.; Wu, J.; Wei, S.; Guo, Z. Advanced Titania Nanostructures and Composites for Lithium Ion Battery. *J. Mater. Sci.* **2012**, *47* (6), 2519–2534.

(12) Hoffmann, M. R.; Martin, S. T.; Choi, W.; Bahnemann, D. W. Environmental Applications of Semiconductor Photocatalysis. *Chem. Rev.* **1995**, *95* (1), 69–96.

(13) Chen, X.; Mao, S. S. Titanium Dioxide Nanomaterials : Synthesis, Properties, Modifications and Applications. *Chem. Rev.* **2007**, *107*, 2891–2959.

(14) Zhang, R.; Elzatahry, A. A.; Al-Deyab, S. S.; Zhao, D. Mesoporous Titania: From Synthesis to Application. *Nano Today* **2012**, *7* (4), 344–366.

(15) Alberius, P. C. A.; Frindell, K. L.; Hayward, R. C.; Kramer, E. J.; Stucky, G. D.; Chmelka, B. F. General Predictive Syntheses of Cubic, Hexagonal, and Lamellar Silica and Titania Mesostructured Thin Films. *Chem. Mater.* **2002**, *14* (8), 3284–3294.

(16) Choi, S. Y.; Mamak, M.; Coombs, N.; Chopra, N.; Ozin, G. A. Thermally Stable Two-Dimensional Hexagonal Mesoporous Nanocrystalline Anatase, Meso-Nc-TiO2: Bulk and Crack-Free Thin Film Morphologies. *Adv. Funct. Mater.* **2004**, *14* (4), 335–344.

(17) Di Paola, A.; Bellardita, M.; Palmisano, L. Brookite, the Least Known TiO_2 Photocatalyst. *Catalysts* **2013**, *3* (1), 36–73.

(18) Yanagisawa, T.; Shimizu, T.; Kuroda, K.; Kato, C. The Preparation of Alkyltrimethylammonium-Kanemite Complexes and Their Conversion to Microporous Materials. *Bull. Chem. Soc. Jpn.* **1990**, *63* (4), 988–992.

(19) Beck, J. S.; Vartuli, J. C.; Roth, W. J.; Leonowicz, M. E.; Kresge, C. T.; Schmitt, K. D.; Chu, C. T. W.; Olson, D. H.; Sheppard, E. W.; McCullen, S. B.; et al. A New Family of Mesoporous Molecular Sieves Prepared with Liquid Crystal Templates. *J. Am. Chem. Soc.* **1992**, *114* (27), 10834–10843.

(20) U.S. Geological Survey. *Mineral Commodity Summaries*; 2017.

(21) Chen, X.; Burda, C. The Electronic Origin of the Visible-Light Absorption Properties of C-, N- and S-Doped TiO_2 Nanomaterials. *J. Am. Chem. Soc.* **2008**, *130* (15), 5018–5019.

(22) Haggerty, J. E. S.; Schelhas, L. T.; Kitchaev, D. A.; Mangum, J. S.; Garten, L. M.; Sun, W.; Stone, K. H.; Perkins, J. D.; Toney, M. F.; Ceder, G.; et al. High-Fraction Brookite Films from Amorphous Precursors. *Sci. Rep.* **2017**, *7* (1), 1–11.

(23) Amtout, A.; Leonelli, R. Optical Properties of Rutile near Its Fundamental Band Gap. *Phys. Rev. B* **1995**, *51* (11), 6842–6851.

(24) Reddy, K. M.; Manorama, S. V.; Reddy, A. R. Bandgap Studies on Anatase Titanium Dioxide Nanoparticles. *Mater. Chem. Phys.* **2003**, *78* (1), 239–245.

(25) Grätzel, M. The Influence of the Crystal Lattice Structure on the Conduction Band Energy of Oxides of Titanium(IV). *Chem. Phys. Lett.* **1985**, *118* (5), 474–477.

(26) Reyes-Coronado, D.; Rodríguez-Gattorno, G.; Espinosa-Pesqueira, M. E.; Cab, C.; De

Coss, R.; Oskam, G. Phase-Pure TiO_2 Nanoparticles: Anatase, Brookite and Rutile. *Nanotechnology* **2008**, *19* (14).

(27) Luttrell, T.; Halpegamage, S.; Tao, J.; Kramer, A.; Sutter, E.; Batzill, M. Why Is Anatase a Better Photocatalyst than Rutile? - Model Studies on Epitaxial TiO_2 Films. *Sci. Rep.* **2015**, *4*, 1–8.

(28) Kho, Y. K.; Iwase, A.; Teoh, W. Y.; Mädler, L.; Kudo, A.; Amal, R. Photocatalytic H_2 Evolution over TiO_2 Nanoparticles. The Synergistic Effect of Anatase and Rutile. *J. Phys. Chem. C* **2010**, *114* (6), 2821–2829.

(29) Li, G.; Chen, L.; Graham, M. E.; Gray, K. A. A Comparison of Mixed Phase Titania Photocatalysts Prepared by Physical and Chemical Methods: The Importance of the Solid-Solid Interface. *J. Mol. Catal. A Chem.* **2007**, *275* (1–2), 30–35.

(30) Scanlon, D. O.; Dunnill, C. W.; Buckeridge, J.; Shevlin, S. A.; Logsdail, A. J.; Woodley, S. M.; Catlow, C. R. A.; Powell, M. J.; Palgrave, R. G.; Parkin, I. P.; et al. Band Alignment of Rutile and Anatase TiO_2. *Nat. Mater.* **2013**, *12* (9), 798–801.

(31) Pfeifer, V.; Erhart, P.; Li, S.; Rachut, K.; Morasch, J.; Brötz, J.; Reckers, P.; Mayer, T.; Rühle, S.; Zaban, A.; et al. Energy Band Alignment between Anatase and Rutile TiO_2. *J. Phys. Chem. Lett.* **2013**, *4* (23), 4182–4187.

(32) Shibata, T.; Irie, H.; Ohmori, M.; Nakajima, A.; Watanabe, T.; Hashimoto, K. Comparison of Photochemical Properties of Brookite and Anatase TiO_2 Films. *Phys. Chem. Chem. Phys.* **2004**, *6* (6), 1359.

(33) Mattsson, A.; Österlund, L. Adsorption and Photoinduced Decomposition of Acetone and Acetic Acid on Anatase, Brookite, and Rutile TiO_2 Nanoparticles. *J. Phys. Chem. C* **2010**, *114* (33), 14121–14132.

(34) Liu, L.; Zhao, H.; Andino, J. M.; Li, Y. Photocatalytic CO_2 Reduction with H_2O on TiO_2 Nanocrystals: Comparison of Anatase, Rutile, and Brookite Polymorphs and Exploration of Surface Chemistry. *ACS Catal.* **2012**, *2* (8), 1817–1828.

(35) Zhao, B.; Chen, F.; Huang, Q.; Zhang, J. Brookite TiO_2 Nanoflowers. *Chem. Commun.* **2009**, No. 34, 5115–5117.

(36) Banfield, J. F.; Veblen, D. R.; Smith, D. J. The Identification of Naturally Occurring Titanium Dioxide (B) by Structure Determination Using High-Resolution Electron Microscopy, Image Simulation, and Distance-Least-Squares Refinement. *Am. Mineral.* **1991**, *76* (3–4), 343–353.

(37) Marchand, R.; Brohan, L.; Tournoux, M. TiO_2(B) a New Form of Titanium Dioxide and

the Potassium Octatitanate K2Ti8O17. *Mater. Res. Bull.* **1980**, *15* (8), 1129–1133.

(38) Liu, Z.; Andreev, Y. G.; Robert Armstrong, A.; Brutti, S.; Ren, Y.; Bruce, P. G. Nanostructured TiO_2(B): The Effect of Size and Shape on Anode Properties for Li-Ion Batteries. *Prog. Nat. Sci. Mater. Int.* **2013**, *23* (3), 235–244.

(39) Zhang, H.; Banfield, J. F. Thermodynamic Analysis of Phase Stability of Nanocrystalline Titania. *J. Mater. Chem.* **1998**, *8* (9), 2073–2076.

(40) Hanaor, D. A. H.; Sorrell, C. C. Review of the Anatase to Rutile Phase Transformation. *J. Mater. Sci.* **2011**, *46* (4), 855–874.

(41) Zhang, H.; Banfield, J. F. Understanding Polymorphic Phase Transformation Behavior during Growth of Nanocrystalline Aggregates: Insights from TiO_2. *J. Phys. Chem. B* **2000**, *104* (15), 3481–3487.

(42) Brinker, C. J.; Scherer, G. W. *Sol-Gel Science*; Academic Press: London, 1990.

(43) Livage, J.; Henry, M.; Sanchez, C. Sol-Gel Chemistry of Transition Metal Oxides. *Prog. Solid State Chem.* **1988**, *18*, 259–341.

(44) Símonarson, G.; Sommer, S.; Lotsari, A.; Elgh, B.; Iversen, B. B.; Palmqvist, A. E. C. Evolution of the Polymorph Selectivity of Titania Formation under Acidic and Low-Temperature Conditions. *ACS Omega* **2019**, *4* (3), 5750–5757.

(45) Kominami, H.; Kohno, M.; Kera, Y. Synthesis of Brookite-Type Titanium Oxide Nano-Crystals in Organic Media. *J. Mater. Chem.* **2000**, *10* (5), 1151–1156.

(46) Pottier, A.; Chanéac, C.; Tronc, E.; Mazerolles, L.; Jolivet, J. P. Synthesis of Brookite TiO2 Nanoparticles by Thermolysis of TiCl4 in Strongly Acidic Aqueous Media. *J. Mater. Chem.* **2001**, *11* (4), 1116–1121.

(47) Simonsen, M. E.; Søgaard, E. G. Sol-Gel Reactions of Titanium Alkoxides and Water: Influence of PH and Alkoxy Group on Cluster Formation and Properties of the Resulting Products. *J. Sol-Gel Sci. Technol.* **2010**, *53* (3), 485–497.

(48) Simonsen, M. E.; Sogaard, E. G. Identification of Ti Clusters during Nucleation and Growth of Sol-Gel-Derived TiO_2 Nanoparticles. *Eur. J. Mass Spectrom.* **2013**, *19*, 265–273.

(49) Iler, R. K. *The Chemistry of Silica*; John Wiley & sons, ltd.: New York, 1979.

(50) Sun, B.; Zhou, G.; Zhang, H. Synthesis, Functionalization, and Applications of Morphology-Controllable Silica-Based Nanostructures: A Review. *Prog. Solid State Chem.* **2016**, *44* (1), 1–19.

(51) Fujishima, A.; Zhang, X.; Tryk, D. A. TiO2 Photocatalysis and Related Surface Phenomena. *Surf. Sci. Rep.* **2008**, *63* (12), 515–582.

(52) Andersson, M.; Birkedal, H.; Franklin, N. R.; Ostomel, T.; Boettcher, S.; Palmqvist, A. E. C.; Stucky, G. D. Ag/AgCl-Loaded Ordered Mesoporous Anatase for Photocatalysis. *Chem. Mater.* **2005**, *17* (6), 1409–1415.

(53) Holmberg, K.; Jönsson, B.; Kronberg, B.; Lindman, B. *Surfactants and Polymers in Aqueous Solution*, 2 ed.; John Wiley & sons, ltd.: Chichester, 2003.

(54) Bagshaw, S. A.; Prouzet, E.; Pinnavaia, T. J. Templating of Mesoporous Molecular Sieves by Nonionic Polyethylene Oxide Surfactants. *Science (80-.).* **1995**, *269* (5228), 1242–1244.

(55) Alexandridis, P.; Lindman, B. *Amphiphilic Block Copolymers: Self-Assembly and Apllications*; Elsevier: Amsterdam, 2000.

(56) Alexandridis, P.; Hatton, T. A. Block Copolymer Surfactants in Aqueous Solutions and at Interface: Thermodynamics, Structure, Dynamics and Modeling. *Colloids Surfaces A Physicochem. Eng. Asp.* **1995**, *96*, 1–46.

(57) Mortensen, K. Structural Studies of Aqueous Solutions of PEO-PPO-PEO Triblock Copolymers, Their Micellar Aggregates and Mesophases; a Small-Angle Neutron Scattering Study. *J. Phys. Condens. Matter* **1996**, *8* (25 SUPPL. A).

(58) Ivanova, R.; Alexandridis, P.; Lindman, B. Interaction of Poloxamer Block Copolymers with Cosolvents and Surfactants. *Colloids Surfaces A Physicochem. Eng. Asp.* **2001**, *183–185*, 41–53.

(59) Tiberg, F.; Lindman, B.; Landgren, M. Interfacial Behaviour of Non-Ionic Surfactants at the Silica-Water Interface Revealed by Ellipsometry. *Thin Solid Films* **1993**, *234* (1–2), 478–481.

(60) Takahashi, R.; Nakanishi, K.; Soga, N. Aggregation Behavior of Alkoxide-Derived Silica in Sol-Gel Process in Presence of Poly(Ethylene Oxide). *J. Sol-Gel Sci. Technol.* **2000**, *17* (1), 7–18.

(61) Iruthayaraj, J.; Poptoshev, E.; Vareikis, A.; Makuška, R.; Van Der Wal, A.; Claesson, P. M. Adsorption of Low Charge Density Polyelectrolyte Containing Poly(Ethylene Oxide) Side Chains on Silica: Effects of Ionic Strength and PH. *Macromolecules* **2005**, *38* (14), 6152–6160.

(62) Brinker, C. J.; Lu, Y.; Sellinger, A.; Fan, H. Evaporation Induced Self-Assembly: Nanostructures Made Easy. *Adv. Mater.* **1999**, *11* (7), 579–585.

(63) Lu, Y.; Fan, H.; Stump, A.; Ward, T. L.; Rieker, T.; Brinker, C. J. Aerosol-Assisted Self-Assembly of Mesostructured Spherical Nanoparticles. *Nature* **1999**, *398*, 223–226.

(64) Zhao, D.; Huo, Q.; Feng, J.; Chmelka, B. F.; Stucky, G. D. Nonionic Triblock and Star Diblock Copolymer and Oligomeric Sufactant Syntheses of Highly Ordered, Hydrothermally Stable, Mesoporous Silica Structures. *J. Am. Chem. Soc.* **1998**, *120* (24), 6024–6036.

(65) Zhao, D.; Feng, J.; Huo, Q.; Melosh, N.; Fredrickson, G. H.; Chmelka, B. F.; Stucky, G. D. Triblock Copolymer Syntheses of Mesoporous Silica with Periodic 50 to 300 Angstrom Pores. *Science (80-.).* **1998**, *279* (5350), 548–552.

(66) Sundblom, A.; Oliveira, C. L. P.; Pedersen, J. S.; Palmqvist, A. E. C. On the Formation Mechanism of Pluronic-Templated Mesostructured Silica. *J. Phys. Chem. C* **2010**, *114* (8), 3483–3492.

(67) Nilsson, E.; Sakamoto, Y.; Palmqvist, A. E. C. Low-Temperature Synthesis and HRTEM Analysis of Ordered Mesoporous Anatase with Tunable Crystallite Size and Pore Shape. *Chem. Mater.* **2011**, *23* (11), 2781–2785.

(68) Smart, L. E.; Moore, E. A. *Solid State Chemistry an Introduction*, 4th ed.; CRC press: Boca Raton, 2012.

(69) Rietveld, H. M. Line Profiles of Neutron Powder-Diffraction Peaks for Structure Refinement. *Acta Crystallogr.* **1967**, *22* (1), 151–152.

(70) Rietveld, H. M. A Profile Refinement Method for Nuclear and Magnetic Structures. *J. Appl. Crystallogr.* **1969**, *2* (2), 65–71.

(71) Rodríguez-Carvajal, J. Recent Advances in Magnetic Structure Determination by Neutron Powder Diffraction. *Phys. B Condens. Matter* **1993**, *192*, 55–69.

(72) Baur, W. H. Über Die Verfeinerung Der Kristallstrukturbestimmung Einiger Vertreter Des Rutiltyps: TiO_2, SnO_2, GeO_2 Und MgF_2. *Acta Crystallogr.* **1956**, *9* (6), 515–520.

(73) Djerdj, I.; Tonejc, A. M. Structural Investigations of Nanocrystalline TiO_2 Samples. *J. Alloys Compd.* **2006**, *413* (1–2), 159–174.

(74) Schnablegger, H.; Singh, Y. The SAXS Guide: Getting Acquainted with the Principles. *Ant. Paar* **2013**, 124.

(75) Henderson, G. S.; Groot, F. M. F. De; Moulton, B. J. A. X-Ray Absorption Near-Edge Structure (XANES) Spectroscopy. *Rev. Mineral. Geochemistry* **2014**, *78*, 75–138.

(76) Cabaret, D.; Bordage, A.; Juhin, A.; Arfaoui, M.; Gaudry, E. First-Principles

Calculations of X-Ray Absorption Spectra at the K-Edge of 3d Transition Metals: An Electronic Structure Analysis of the Pre-Edge. *Phys. Chem. Chem. Phys.* **2010**, *12* (21), 5619–5633.

(77) Luca, V.; Djajanti, S.; Howe, R. F. Structural and Electronic Properties of Sol−Gel Titanium Oxides Studied by X-Ray Absorption Spectroscopy. *J. Phys. Chem. B* **2002**, *102* (52), 10650–10657.

(78) Leitzke, F. P.; Fonseca, R. O. C.; Göttlicher, J.; Steininger, R.; Jahn, S.; Prescher, C.; Lagos, M. Ti K-Edge XANES Study on the Coordination Number and Oxidation State of Titanium in Pyroxene, Olivine, Armalcolite, Ilmenite, and Silicate Glass during Mare Basalt Petrogenesis. *Contrib. to Mineral. Petrol.* **2018**, *173* (12), 1–17.

(79) Jalilehvand, F. Structure of Hydrated Ions and Cyanide Complexes by X-Ray Absorption Spectroscopy, PhD. Thesis, KTH Stockholm, Sweden, 2000.

(80) Rehr, J. J.; Ankudinov, A.; Zabinsky, S. I. New Developments in NEXAFS/EXAFS Theory. *Catal. Today* **1998**, *39*, 263–269.

(81) Klementiev, K.; Norén, K.; Carlson, S.; Sigfridsson Clauss, K. G. V.; Persson, I. The BALDER Beamline at the MAX IV Laboratory. *J. Phys. Conf. Ser.* **2016**, *712* (1), 8–12.

(82) Kothleitner, G.; Hofer, F. Optimization of the Signal to Noise Ratio in EFTEM Elemental Maps with Regard to Different Eonization Edge Types. *Micron* **1998**, *29* (5), 349–357.

(83) Bard, A. J.; Faulkner, L. R. *Electrochemical Methods*, 2nd ed.; John Wiley & sons, ltd., 2001.

(84) De Klerk, N. J. J.; Vasileiadis, A.; Smith, R. B.; Bazant, M. Z.; Wagemaker, M. Explaining Key Properties of Lithiation in TiO_2 -Anatase Li-Ion Battery Electrodes Using Phase-Field Modeling. *Phys. Rev. Mater.* **2017**, *1* (2), 1–13.

(85) Elgh, B.; Yuan, N.; Cho, H. S.; Nilsson, E.; Terasaki, O.; Palmqvist, A. E. C. Correlating Photocatalytic Performance with Microstructure of Mesoporous Titania Influenced by Employed Synthesis Conditions. *J. Phys. Chem. C* **2013**, *117* (32), 16492–16499.

(86) Elgh, B.; Yuan, N.; Cho, H. S.; Magerl, D.; Philipp, M.; Roth, S. V.; Yoon, K. B.; Müller-Buschbaum, P.; Terasaki, O.; Palmqvist, A. E. C. Controlling Morphology, Mesoporosity, Crystallinity, and Photocatalytic Activity of Ordered Mesoporous TiO2 Films Prepared at Low Temperature. *APL Mater.* **2014**, *2* (11), 113313.

(87) Elgh, B.; Palmqvist, A. E. C. Controlling Anatase and Rutile Polymorph Selectivity during Low-Temperature Synthesis of Mesoporous TiO_2 Films. *J. Mater. Chem. A* **2014**,

2 (9), 3024.

(88) Holmqvist, P.; Alexandridis, P.; Lindman, B. Modification of the Microstructure in Block Copolymer−water−"Oil" Systems by Varying the Copolymer Composition and the "Oil" Type: Small-Angle X-Ray Scattering and Deuterium-NMR Investigation. *J. Phys. Chem. B* **1998**, *102* (7), 1149–1158.

(89) Hannan, M. A.; Lipu, M. S. H.; Hussain, A.; Mohamed, A. A Review of Lithium-Ion Battery State of Charge Estimation and Management System in Electric Vehicle Applications: Challenges and Recommendations. *Renew. Sustain. Energy Rev.* **2017**, *78*, 834–854.

(90) Wang, Y.; Liu, B.; Li, Q.; Cartmell, S.; Ferrara, S.; Deng, Z. D.; Xiao, J. Lithium and Lithium Ion Batteries for Applications in Microelectronic Devices: A Review. *J. Power Sources* **2015**, *286*, 330–345.

(91) Müller, M.; Viernstein, L.; Truong, C. N.; Eiting, A.; Hesse, H. C.; Witzmann, R.; Jossen, A. Evaluation of Grid-Level Adaptability for Stationary Battery Energy Storage System Applications in Europe. *J. Energy Storage* **2017**, *9*, 1–11.

(92) Zubi, G.; Dufo-López, R.; Carvalho, M.; Pasaoglu, G. The Lithium-Ion Battery: State of the Art and Future Perspectives. *Renew. Sustain. Energy Rev.* **2018**, *89*, 292–308.

(93) Larcher, D.; Tarascon, J. M. Towards Greener and More Sustainable Batteries for Electrical Energy Storage. *Nat. Chem.* **2015**, *7* (1), 19–29.

(94) Kaskhedikar, N. A.; Maier, J. Lithium Storage in Carbon Nanostructures. *Adv. Mater.* **2009**, *21* (25–26), 2664–2680.

(95) Nitta, N.; Wu, F.; Lee, J. T.; Yushin, G. Li-Ion Battery Materials : Present and Future. *Mater. Today* **2015**, *18* (5), 252–264.

(96) Kasavajjula, U.; Wang, C.; Appleby, A. J. Nano- and Bulk-Silicon-Based Insertion Anodes for Lithium-Ion Secondary Cells. *J. Power Sources* **2007**, *163* (2), 1003–1039.

(97) Winter, M.; Besenhard, J. O. Electrochemical Lithiation of Tin and Tin-Based Intermetallics and Composites. *Electrochim. Acta* **1999**, *45* (1), 31–50.

(98) Wagemaker, M.; Kearley, G. J.; Van Well, A. A.; Mutka, H.; Mulder, F. M. Multiple Li Positions inside Oxygen Octahedra in Lithiated TiO2 Anatase. *J. Am. Chem. Soc.* **2003**, *125* (3), 840–848.

(99) Liang, J.; Wang, Z.; Li, Z.; Wang, X.; Yu, K. Fabrication of Nanostructured TiO2 Using a Solvothermal Reaction for Lithium-Ion Batteries. *Nanomater. Nanotechnol.* **2016**, *6* (1), 1–8.

(100) Liu, J.; Kopold, P.; vanAken, P. A.; Maier, J.; Yu, Y. Energy Storage Materials from Nature through Nanotechnology: A Sustainable Route from Reed Plants to a Silicon Anode for Lithium-Ion Batteries. *Angew. Chemie - Int. Ed.* **2015**, *54* (33), 9632–9636.

(101) Zhang, W.-M.; Hu, J.-S.; Guo, Y.-G.; Zheng, S.-F.; Zhong, L.-S.; Song, W.-G.; Wan, L.-J. Tin-Nanoparticles Encapsulated in Elastic Hollow Carbon Spheres for High-Performance Anode Material in Lithium-Ion Batteries. *Adv. Mater.* **2008**, *20* (6), 1160–1165.

(102) Deng, Y.; Fang, C.; Chen, G. The Developments of SnO2/Graphene Nanocomposites as Anode Materials for High Performance Lithium Ion Batteries: A Review. *J. Power Sources* **2016**, *304*, 81–101.

(103) Zuo, X.; Zhu, J.; Müller-Buschbaum, P.; Cheng, Y. J. Silicon Based Lithium-Ion Battery Anodes: A Chronicle Perspective Review. *Nano Energy* **2017**, *31*, 113–143.

(104) Liu, Y.; Yang, Y. Recent Progress of TiO_2-Based Anodes for Li Ion Batteries. *J. Nanomater.* **2016**, *2016* (2).

(105) Lim, E.; Shim, H.; Fleischmann, S.; Presser, V. Fast and Stable Lithium-Ion Storage Kinetics of Anatase Titanium Dioxide/Carbon Onion Hybrid Electrodes. *J. Mater. Chem. A* **2018**, *6* (20), 9480–9488.

(106) Kim, J.; Cho, J. Rate Characteristics of Anatase TiO_2 Nanotubes and Nanorods for Lithium Battery Anode Materials at Room Temperature. *J. Electrochem. Soc.* **2007**, *154* (6), A542–A546.

(107) Hu, Y. S. H.; Kienle, L.; Guo, Y. G.; Maier, J. High Lithium Electroactivity of Nanometer-Sized Rutile TiO_2. *Adv. Mater.* **2006**, *18* (11), 1421–1426.

(108) Reddy, M. A.; Kishore, M. S.; Pralong, V.; Caignaert, V.; Varadaraju, U. V.; Raveau, B. Room Temperature Synthesis and Li Insertion into Nanocrystalline Rutile TiO_2. *Electrochem. commun.* **2006**, *8* (8), 1299–1303.

(109) Dylla, A. G.; Henkelman, G.; Stevenson, K. J. Lithium Insertion in Nanostructured TiO_2(B) Architectures. *Acc. Chem. Res.* **2013**, *46* (5), 1104–1112.

(110) Ren, Y.; Liu, Z.; Pourpoint, F.; Armstrong, A. R.; Grey, C. P.; Bruce, P. G. Nanoparticulate TiO_2(B): An Anode for Lithium-Ion Batteries. *Angew. Chemie - Int. Ed.* **2012**, *51* (9), 2164–2167.

(111) Borghols, W. J. H.; Lützenkirchen-Hecht, D.; Haake, U.; Chan, W.; Lafont, U.; Kelder, E. M.; van Eck, E. R. H.; Kentgens, A. P. M.; Mulder, F. M.; Wagemaker, M. Lithium Storage in Amorphous TiO_2 Nanoparticles. *J. Electrochem. Soc.* **2010**, *157* (5), A582–

A588.

(112) Ryu, W. H.; Nam, D. H.; Ko, Y. S.; Kim, R. H.; Kwon, H. S. Electrochemical Performance of a Smooth and Highly Ordered TiO_2 Nanotube Electrode for Li-Ion Batteries. *Electrochim. Acta* **2012**, *61*, 19–24.

(113) Mi, J. L.; Jensen, K. M. Ø.; Tyrsted, C.; Bremholm, M.; Iversen, B. B. In Situ Total X-Ray Scattering Study of the Formation Mechanism and Structural Defects in Anatase TiO_2 Nanoparticles under Hydrothermal Conditions. *CrystEngComm* **2015**, *17* (36), 6868–6877.

(114) Zhang, H.; Chen, B.; Banfield, J. F.; Waychunas, G. A. Atomic Structure of Nanometer-Sized Amorphous TiO_2. *Phys. Rev. B - Condens. Matter Mater. Phys.* **2008**, *78* (21), 1–12.

(115) Moitzheim, S.; De Gendt, S.; Vereecken, P. M. Investigation of the Li-Ion Insertion Mechanism for Amorphous and Anatase TiO_2 Thin-Films. *J. Electrochem. Soc.* **2019**, *166* (2), A1–A9.

(116) Gogotsi, Y.; Penner, R. M. Energy Storage in Nanomaterials – Capacitive, Pseudocapacitive, or Battery-Like? *ACS Nano* **2018**, *12* (3), 2081–2083.

(117) Ivanova, R.; Lindman, B.; Alexandridis, P. Effect of Pharmaceutically Acceptable Glycols on the Stability of the Liquid Crystalline Gels Formed by Poloxamer 407 in Water. *J. Colloid Interface Sci.* **2002**, *252* (1), 226–235.

(118) Ivanova, R.; Lindman, B.; Alexandridis, P. Effect of Glycols on the Self-Assembly of Amphiphilic Block Copolymers in Water. 1. Phase Diagrams and Structure Identification. *Langmuir* **2000**, *16* (8), 3660–3675.